Supplementary Information: Building hurricane-resilient urban grid by climate-informed system hardening optimization

Shuo Li[1,2,+], Dong Liu[2,+], Qianyu Zhao[1,*], Shouxiang Wang[1,*], and Chi K. Tse[2,*]

[1] *State key laboratory of Intelligent Power Distribution Equipment and System, Tianjin University, Tianjin, China*

[2] *Department of Electrical Engineering, City University of Hong Kong, Hong Kong*

[*] *corresponding.author@email.example*

[+] *these authors contributed equally to this work*

Supplementary Notes

Supplementary Tables

Supplementary Figures

Supplementary Note 1: Synthetic low voltage distribution network

The synthesis of realistic low-voltage distribution networks represents a critical foundation for climate-informed resilience analysis, as these networks form the final connection between the electrical grid and end-use consumers. We model synthetic low-voltage distribution systems as collections of radial tree-structured subnetworks, where each tree is rooted at a pole-mounted distribution transformers and terminates at individual power load nodes. This hierarchical architecture reflects the predominant configuration of overhead distribution systems in urban and suburban environments, as shown in Supplementary Figure 1a. Given that distribution transformers in overhead systems are typically mounted on utility poles positioned along roadway corridors, we leverage high-resolution geographic data from OpenStreetMap (OSM) to establish the spatial relationship between power demand locations and feasible infrastructure placement sites [1].

For each road segment $(i, j) \in \mathcal{E}_R$ within the street network of a given study area, we construct a candidate connectivity graph $\mathcal{G}_S(\mathcal{V}_S, \mathcal{E}_S)$, where the vertex set $\mathcal{V}_S$ comprises potential transformer locations $\mathcal{V}_T$ (corresponding to utility pole positions along roadways) and load connection points $\mathcal{V}_L$ (representing residential, commercial, and industrial power demand nodes). The edge set $\mathcal{E}_S$ captures all feasible electrical connections between these vertices, constructed using either fully connected topologies for small networks or computationally efficient Delaunay triangulations for larger urban areas to maintain realistic connectivity patterns while preserving computational efficiency [1].

The optimization objective seeks to determine the optimal network topology $\mathcal{G}_D(\mathcal{V}_D, \mathcal{E}_D)$, where $\mathcal{V}_D$ contains the selected transformer locations $\mathcal{V}_T^*$ and all load points $\mathcal{V}_L$, while $\mathcal{E}_D$ represents the final distribution line configuration. This combinatorial optimization problem is formulated as a mixed-integer linear programming (MILP) model that minimizes total network construction cost while satisfying operational and topological constraints inherent to radial distribution systems:

$$\min_{x} \quad \sum_{(i,j)\in\mathcal{E}_S} w_{ij} x_{ij} \tag{1}$$

$$\sum_{\{j|(l,j)\in\mathcal{E}_S\}} x_{lj} \leq 2, \quad \forall l \in \mathcal{V}_L \tag{2}$$

$$\sum_{j\in\mathcal{N}(i)} P_{ij} = P_i^L, \quad \forall i \in \mathcal{V}_L \tag{3}$$

$$-\underline{P}_{ij} x_{ij} \leq P_{ij} \leq \overline{P}_{ij} x_{ij}, \quad \forall (i,j) \in \mathcal{E}_S \tag{4}$$

$$\sum_{(i,j)\in\mathcal{E}_S} x_{ij} = |\mathcal{V}_L| \tag{5}$$

where x_{ij} is a binary decision variable that equals 1 if edge (i, j) is included in the optimal network configuration and 0 otherwise, P_{ij} represents the power flow along edge (i, j) in kilowatts, w_{ij} denotes the geodesic distance between nodes i and j in meters, P_i^L represents the power demand at load node i in kilowatts, $\underline{P}_{ij}$ and $\overline{P}_{ij}$ are the lower and upper bounds on power flow capacity for edge (i, j) respectively, and $\mathcal{N}(i)$ represents the set of neighboring nodes connected to node i.

The constraint set enforces realistic network characteristics essential for distribution system operation. Constraint (2) limits each load node to at most two connections, reflecting the degree constraint of a typical radial distribution network [2]. Constraint (3) ensures power flow conservation at each load node, maintaining power balance throughout the network. Constraint (4) couples continuous power flow variables with discrete topology decisions through capacity bounds, ensuring that power can only flow along selected edges. Constraint (5) maintains the fundamental radial topology by ensuring the total number of edges equals the number of load nodes, preventing the formation of loops that would violate standard distribution system operation.

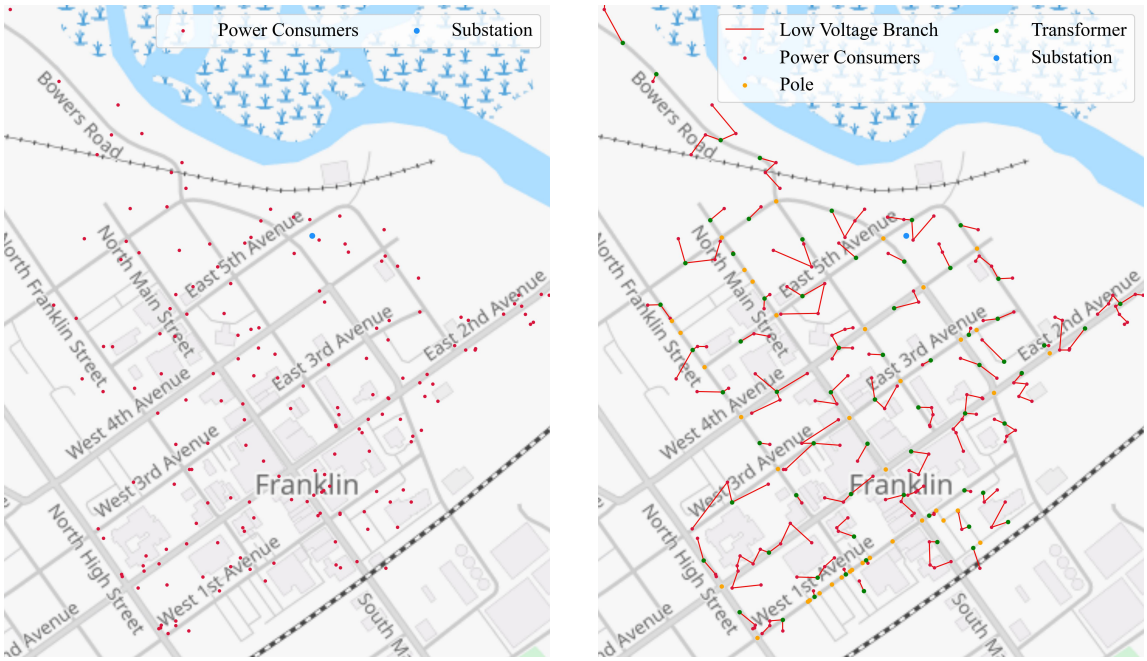

(a) (b)

Supplementary Figure 1: Methodology for synthetic low-voltage distribution network generation. (a), Geographic distribution of electrical loads mapped to street infrastructure in Franklin, Virginia, showing the spatial relationship between power demand locations and potential transformer placement sites derived from OpenStreetMap utility pole data. (b), Example of the resulting synthetic low-voltage distribution network featuring overhead line architecture, where optimally positioned transformers serve as root nodes for radial tree-structured subnetworks operating at 208–480 V distribution voltage levels.

To enhance model realism, we implement several refinements to the basic optimization framework. For potential inter-transformer connections, we set $w_{ij} = \infty$ to prevent parallel transformer installations, which would violate standard utility practice and create unnecessary redundancy. For connections requiring road crossings or traversing challenging terrain, we apply distance penalties to w_{ij} that reflect the additional construction complexity and regulatory requirements associated with such installations. The resulting synthetic low-voltage networks, as demonstrated in Supplementary Figure 1b, exhibit realistic topological properties consistent with actual utility distribution systems: radial operation, appropriate load density, and infrastructure placement aligned with existing transportation corridors. This methodology enables the generation of large-scale urban power distribution networks models necessary for comprehensive climate resilience analyses while maintaining the geographic fidelity required for accurate wind field impact assessment.

Supplementary Note 2: Synthetic medium voltage and high voltage distribution network

The medium-voltage (MV) network serves as the critical interconnect between low-voltage distribution transformers and high-voltage substations, operating at 6–11 kV voltage levels and requiring optimization to minimize infrastructure costs while maintaining operational reliability. We employ Voronoi tessellation to partition the service territory based on aggregate load demand, systematically assigning each optimized transformer node $\mathcal{V}_T^*$ from the low-voltage synthesis phase to its nearest substation $\mathcal{S}$ [3]. This geographic partitioning ensures balanced load distribution across substations while respecting practical service territory boundaries. Within each partition, we construct an undirected candidate graph $\mathcal{G}_R(\mathcal{V}, \mathcal{E}_R)$, where the vertex set $\mathcal{V}$ encompasses both optimized transformer locations $\mathcal{V}_T^*$ and potential pole placement sites $\mathcal{V}_R$ derived from the road network infrastructure.

The optimization objective seeks to identify the minimal-cost network topology $\mathcal{G}_P(\mathcal{V}_P, \mathcal{E}_P)$, where $\mathcal{V}_P$ comprises the selected pole locations $\mathcal{V}_R^*$ and transformer connection points $\mathcal{V}_T^*$. This network design problem is formulated as a mixed-integer linear programming (MILP) model that simultaneously opti-

mizes pole placement and feeder routing decisions while ensuring radial operation and voltage security constraints. The mathematical formulation minimizes total network construction cost while enforcing structural and operational constraints essential for reliable distribution system operation:

$$\min_{u,y,z} \sum_{(i,j)\in\mathcal{E}_R} u_{ij} w_{ij} + \sum_{r\in\mathcal{V}_R} z_r d_r \tag{6}$$

$$z_r \leq y_r, \quad \forall r \in \mathcal{V}_R \tag{7}$$

$$\sum_{\{j|j\in\mathcal{E}_{R,r}\}} u_{rj} \geq y_r, \quad \forall r \in \mathcal{V}_R \tag{8}$$

$$2(y_r - z_r) \leq \sum_{\{j|j\in\mathcal{E}_{R,r}\}} u_{ij} \leq \mid \mathcal{E}_{R,r} \mid y_r, \quad \forall r \in \mathcal{V}_R \tag{9}$$

$$\sum_{(i,j)\in\mathcal{E}_R} u_{ij} = \mid \mathcal{V}_T^* \mid + \sum_{r\in\mathcal{V}_R} y_r - \sum_{r\in\mathcal{V}_R} z_r \tag{10}$$

$$\sum_{\{j|j\in\mathcal{E}_{R,i}^{up}\}} P_{ij} - \sum_{\{j|j\in\mathcal{E}_{R,i}^{dn}\}} P_{ij} = \sum_{\{l|l\in\mathcal{V}_L^i\}} P_l^L, \quad \forall i \in \mathcal{V}_T^* \tag{11}$$

$$-\overline{P}_{ij} z_i \leq \sum_{\{j|j\in\mathcal{E}_{R,i}^{up}\}} P_{ij} - \sum_{\{j|j\in\mathcal{E}_{R,i}^{dn}\}} P_{ij} \leq \overline{P}_{ij} z_i, \quad \forall i \in \mathcal{V}_R \tag{12}$$

$$-M(1-u_{ij}) + \frac{r_{ij}P_{ij} + x_{ij}Q_{ij}}{V_0} \leq V_i - V_j \leq M(1-u_{ij}) + \frac{r_{ij}P_{ij} + x_{ij}Q_{ij}}{V_0}, \quad \forall (i,j) \in \mathcal{E}_R \tag{13}$$

$$-\overline{P}_{ij} u_{ij} \leq P_{ij} \leq \overline{P}_{ij} u_{ij}, \quad \forall (i,j) \in \mathcal{E}_R \tag{14}$$

$$\underline{V}_i \leq V_i \leq \overline{V}_i, \quad \forall i \in \mathcal{V} \tag{15}$$

where u_{ij} is a binary decision variable indicating edge inclusion in the final network topology (1 if edge (i,j) is selected, 0 otherwise), y_r is a binary variable indicating pole utilization at location r (1 if pole is installed, 0 otherwise), z_r is a binary variable designating root node status for medium-voltage feeders (1 if node r serves as a feeder root, 0 otherwise), w_{ij} represents the geodesic distance between nodes i and j serving as edge construction cost, d_r denotes the installation cost for pole at location r, P_{ij} and Q_{ij} represent active and reactive power flows along edge (i,j) respectively, V_i and V_j are voltage magnitudes at nodes i and j, $\mathcal{E}_{R,r}$ is the set of edges incident to node r, $\mathcal{E}_{R,i}^{up}$ and $\mathcal{E}_{R,i}^{dn}$ represent upstream and downstream edges connected to node i, $\mathcal{V}_L^i$ denotes the set of load nodes served by transformer i, P_l^L is the active power demand at load node l, r_{ij} and x_{ij} are resistance and reactance of edge (i,j), V_0 is the reference voltage, M is a sufficiently large constant for big-M constraints, $\overline{P}_{ij}$ represents the power flow capacity limit for edge (i,j), and $\underline{V}_i$ and $\overline{V}_i$ are the lower and upper voltage bounds at node i.

The constraint framework ensures network feasibility through several key mechanisms that reflect standard distribution system operation principles. Constraint (7) establishes logical consistency between root node selection and pole utilization, ensuring that only installed poles can serve as feeder origins. Constraints (8) and (9) enforce proper connectivity requirements for utilized poles, guaranteeing that installed poles have appropriate edge connections while maintaining degree constraints consistent with radial operation. Constraint (10) maintains tree topology by balancing total edge count with node utilization, preventing the formation of loops that would violate radial distribution system principles. Constraint (11) ensures power flow conservation at transformer nodes, maintaining power balance throughout the medium-voltage network. Constraints (12), (13), and (14) couple power flow variables with topology decisions through capacity limits and voltage drop calculations, ensuring that selected network configurations can support required power flows while maintaining voltage quality. Constraint (15) maintains voltage levels within operational limits specified by utility standards and regulatory requirements.

The resulting medium-voltage distribution network, predominantly consisting of overhead lines as shown in Supplementary Figure **2**a, demonstrates realistic radial feeder configurations connecting low-voltage transformers to substations through strategically placed utility poles. The integrated high-voltage distribution network, illustrated in Supplementary Figure **2**b, provides the backbone infrastructure necessary for bulk power delivery across the urban service territory.

Building upon this hierarchical network synthesis framework, we developed detailed topological models for 12 hurricane-prone urban power distribution networks across Virginia, as depicted in Supplementary Figure 3a to 3l. These synthetic networks capture realistic infrastructure characteristics including overhead line vulnerabilities, substation dependencies, and load distribution patterns essential for climate-informed resilience assessment. The geographic diversity of these networks, spanning coastal cities like Norfolk and Chesapeake to inland communities such as Prince George and Southampton, provides comprehensive representation of the hurricane exposure gradients examined in our resilience analysis. Each network model incorporates city-specific load profiles, terrain characteristics, and infrastructure constraints derived from real geographic and demographic data, enabling accurate assessment of hurricane impacts across diverse urban environments.

(a) (b)

Supplementary Figure 2: Hierarchical synthesis of medium and high voltage distribution infrastructure for climate resilience analysis. (a) Optimized medium voltage distribution network showing radial feeder configuration connecting low-voltage transformers to substations through strategic pole placement and routing optimization. (b) Integrated high voltage distribution network providing bulk power delivery by distribution substations across the regional service territory, forming the backbone infrastructure for urban electricity supply.

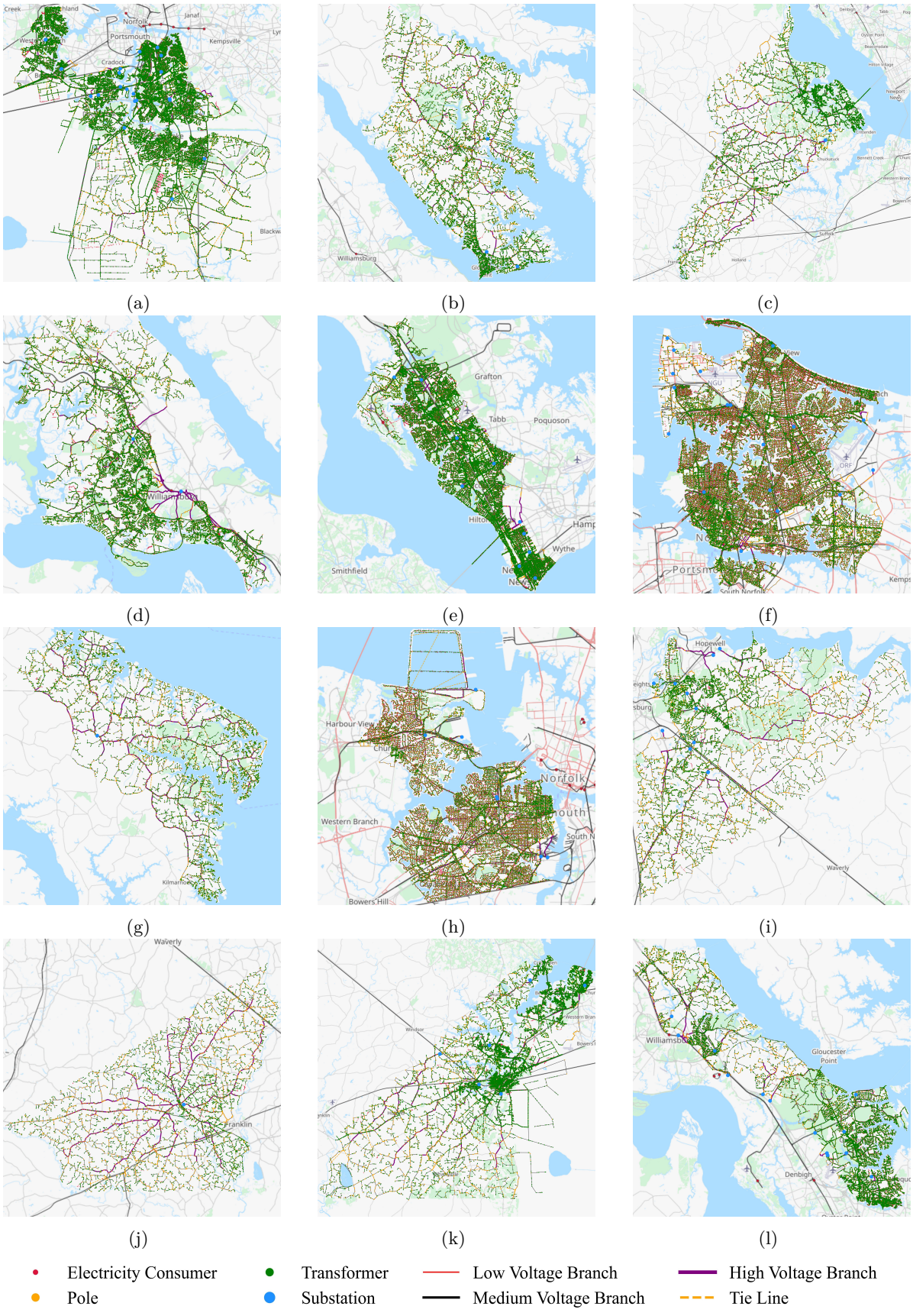

Supplementary Figure 3: Urban-scale power distribution network topologies for hurricane resilience analysis across Virginia cities at risk for hurricanes. Synthetic networks capture realistic infrastructure characteristics including overhead line vulnerabilities, substation dependencies, and load distribution patterns essential for climate-informed resilience assessment. (a) Chesapeake, (b) Gloucester, (c) Isle of Wight, (d) James City, (e) Newport News, (f) Norfolk, (g) Northumberland, (h) Portsmouth, (i) Prince George, (j) Southampton, (k) Suffolk, (l) York.

Supplementary Note 3: Critical infrastructure classification and load prioritization for hurricane resilience assessment

Accurate identification and prioritization of critical infrastructure loads represents a fundamental requirement for climate-informed resilience planning, as these facilities demand prioritized restoration during post-hurricane recovery operations and exhibit disproportionate societal impacts when disrupted. We leverage the comprehensive OpenStreetMap (OSM) geospatial database to systematically classify electrical loads based on their associated building functions and emergency management priorities. The OSM framework employs a hierarchical tagging system that categorizes geographic entities through structured metadata, enabling precise identification of healthcare facilities, emergency services, educational institutions, government operations, and other critical infrastructure types essential for community resilience during extreme weather events.

Our methodology establishes spatial correspondence between electrical load nodes in the synthetic distribution networks and OSM building classifications through a proximity-based matching algorithm that incorporates geometric constraints reflecting realistic utility service patterns. For each electrical load node L in the distribution network, we identify the most appropriate building classification by solving a constrained nearest-neighbor optimization problem within a predefined search radius r. This approach ensures that load classifications reflect actual building functions while maintaining computational efficiency for large-scale urban power distribution networks. The optimal tag assignment $S_T(L)$ is determined through the following optimization:

$$S_T(L) \;=\; \arg \min_{T \,\in\, \{T \,\mid\, d(L,T) \,\leq\, r\}} \{d(L,T) \mid \text{side}(L,T)\}\,, \tag{16}$$

where $d(L,T)$ represents the Euclidean distance between electrical load node L and OSM building tag T, r denotes the maximum search radius for building identification (typically set to 50 meters to capture realistic service connection distances), and the constraint $\text{side}(L,T)$ ensures spatial consistency by requiring both the load node and associated building to lie on the same side of the roadway infrastructure.

The geometric constraint $\text{side}(L,T)$ reflects the realistic spatial relationship between utility service connections and building locations in overhead distribution systems, where electrical service typically connects buildings directly from utility infrastructure on the same side of the street. This constraint prevents erroneous load-building associations that would violate standard utility service practices and ensures that our synthetic networks accurately represent real-world connectivity patterns. The proximity-based approach, illustrated in Supplementary Figure 4 for Franklin, Virginia, demonstrates the automated building classification process and its integration with distribution network topology.

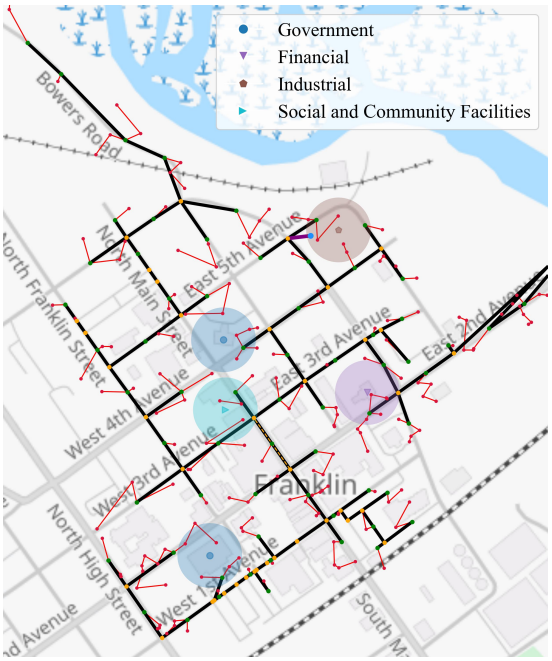

Supplementary Figure 4: Critical infrastructure identification through automated geospatial mapping methodology. Example demonstration of the proximity-based building classification process in Franklin, Virginia, showing how electrical load nodes are systematically matched to OpenStreetMap building types based on distance optimization and geometric constraints, enabling accurate identification of hurricane-vulnerable critical facilities for prioritized resilience planning.

Building upon the geospatial mapping results, we implement a quantitative criticality weighting system that reflects established emergency management priorities and utility restoration practices informed by historical hurricane impact assessments[4;5]. The weighting scheme, detailed in Supplementary Table 1, assigns maximum priority to life-safety facilities such as healthcare centers and emergency services (weight = 20), followed by essential government operations and water treatment facilities (weight = 18), with decreasing weights for transportation hubs, educational institutions, and commercial establishments. This hierarchical prioritization enables quantitative assessment of hurricane impact severity by weighting load losses according to their societal importance, thereby providing a more accurate representation of disaster consequences than simple aggregate outage metrics.

The comprehensive critical infrastructure mapping across all 12 Virginia coastal cities, presented in Supplementary Figure 5a to 5l, reveals heterogeneous patterns of critical facility distribution that reflect varying urban development patterns and demographic characteristics. These spatial distributions inform targeted resilience strategies for hurricane preparedness, enabling planners to prioritize infrastructure hardening and distributed generation placement based on actual critical facility locations rather than uniform assumptions. The resulting load prioritization framework provides essential input for the resilient plan, ensuring that resilience planning decisions account for the differential societal impacts of infrastructure disruptions during extreme weather events.

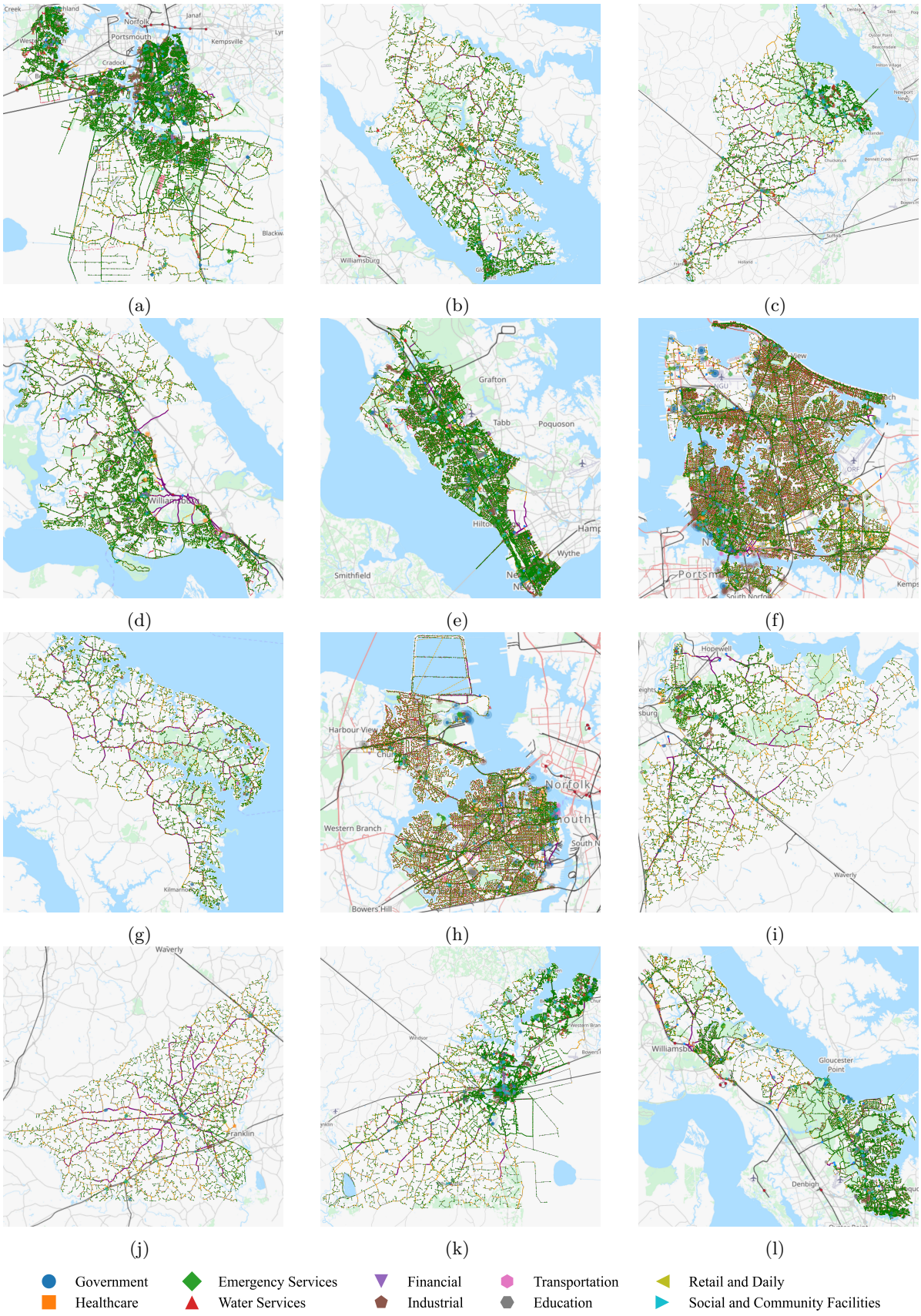

Supplementary Figure 5: Regional distribution of critical infrastructure loads across Virginia coastal cities examined in hurricane resilience analysis. Geospatial mapping reveals heterogeneous patterns of critical facility distribution, informing development of targeted resilience strategies for hurricane preparedness. (a) Chesapeake, (b) Gloucester, (c) Isle of Wight, (d) James City, (e) Newport News, (f) Norfolk, (g) Northumberland, (h) Portsmouth, (i) Prince George, (j) Southampton, (k) Suffolk, (l) York.

Supplementary Table 1: Quantitative weighting scheme for critical infrastructure categories based on emergency management priorities and societal impact severity during hurricane events. Weights reflect established utility restoration practices and life-safety considerations, with maximum priority assigned to healthcare and emergency services facilities.

Infrastructure Category	Weight	Infrastructure Category	Weight
Healthcare Facilities	20	Educational Institutions	12
Emergency Services	20	Financial Services	12
Government Operations	18	Industrial Facilities	10
Water Treatment Services	18	Community Centers	6
Transportation Hubs	14	Retail and Commercial	4

Supplementary Note 4: Geospatial data integration for climate-informed distribution network characterization

Comprehensive assessment of hurricane impacts on electrical distribution infrastructure requires detailed integration of geophysical and environmental data to capture spatially heterogeneous vulnerability patterns across diverse terrain and land-use conditions. The complex interaction between hurricane dynamics and local geography creates highly variable risk profiles that cannot be adequately represented through simplified uniform assumptions. We systematically enhance our synthetic distribution networks with high-resolution geospatial attributes derived from authoritative federal datasets, enabling accurate climate-infrastructure impact modeling that reflects real-world environmental heterogeneity and terrain-dependent vulnerability characteristics.

Topographic characterization represents a critical component of hurricane vulnerability assessment, as elevation directly influences flood risk, storm surge exposure, and terrain-modified wind patterns during extreme weather events. We integrate elevation characteristics using the United States Geological Survey (USGS) 3D Elevation Program's 1/3 arc-second Digital Elevation Model [6], providing 10-meter spatial resolution terrain data across all study regions. Each infrastructure component—including utility poles, distribution transformers, substations, and electrical load nodes—is assigned precise elevation values through bilinear interpolation from the DEM grid to ensure accurate representation of local topographic variations.

Land cover classification provides essential environmental context for understanding how local surface conditions modify hurricane impact mechanisms and infrastructure vulnerability patterns. We incorporate comprehensive land-use data using the National Land Cover Database (NLCD) 2023 dataset [7], which provides standardized 30-meter resolution land-cover categorization across the continental United States through systematic remote sensing analysis. Each network component inherits land cover attributes from its geographic location through spatial overlay operations, enabling differentiation of infrastructure vulnerability based on surrounding environmental conditions. The multi-source geospatial integration creates comprehensive, high-fidelity distribution network models that capture complex interactions between electrical infrastructure and environmental conditions, as demonstrated in Supplementary Figures 6 and 7 for representative Virginia coastal cities.

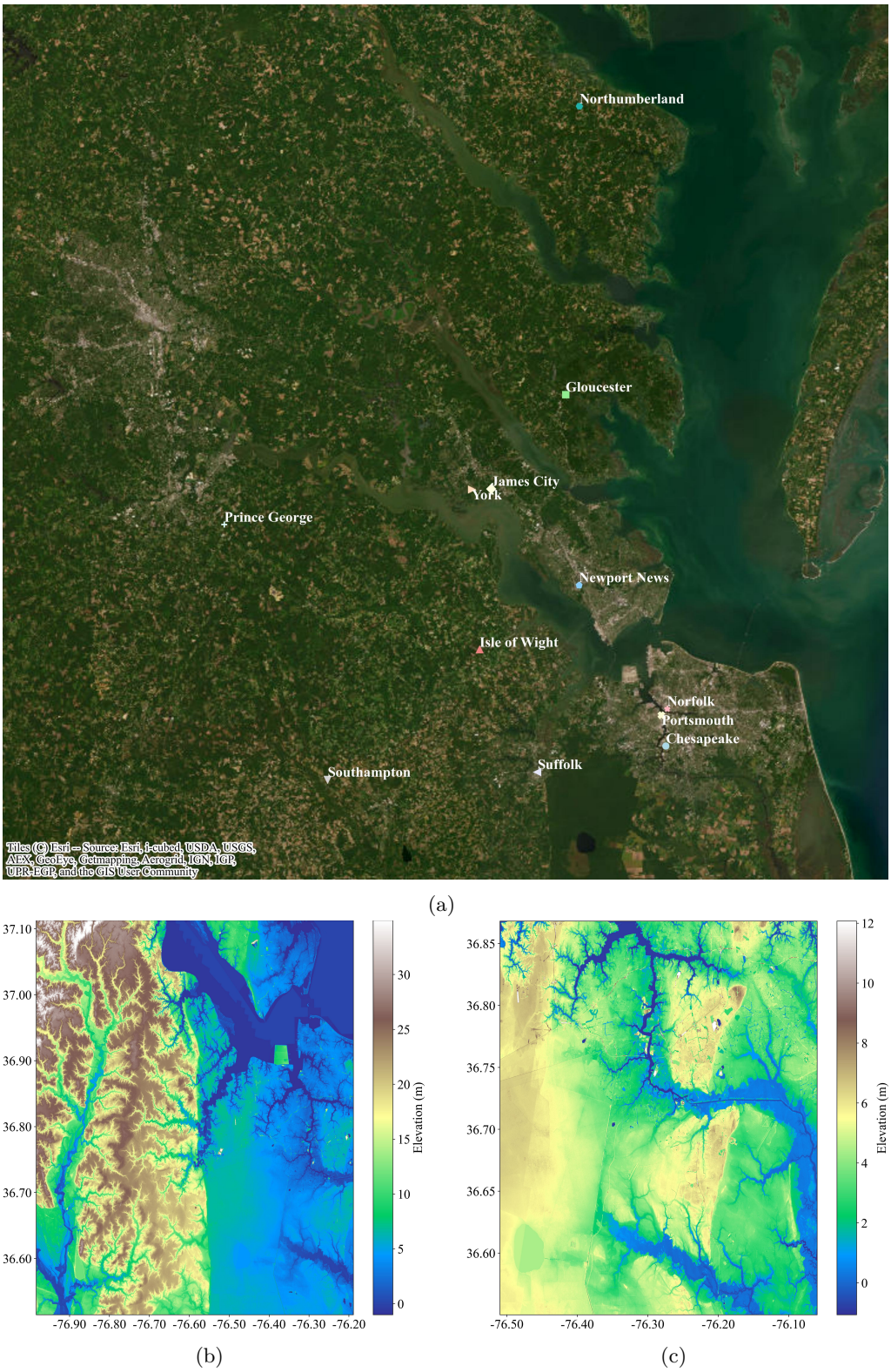

Supplementary Figure 6: Topographic characterization of distribution infrastructure for hurricane vulnerability assessment using USGS 3D Elevation Program data. (a) Regional overview shows elevation gradients across Virginia coastal counties, with detailed network overlays for (b) Suffolk and (c) Chesapeake demonstrating how terrain variations influence infrastructure placement and hurricane risk exposure.

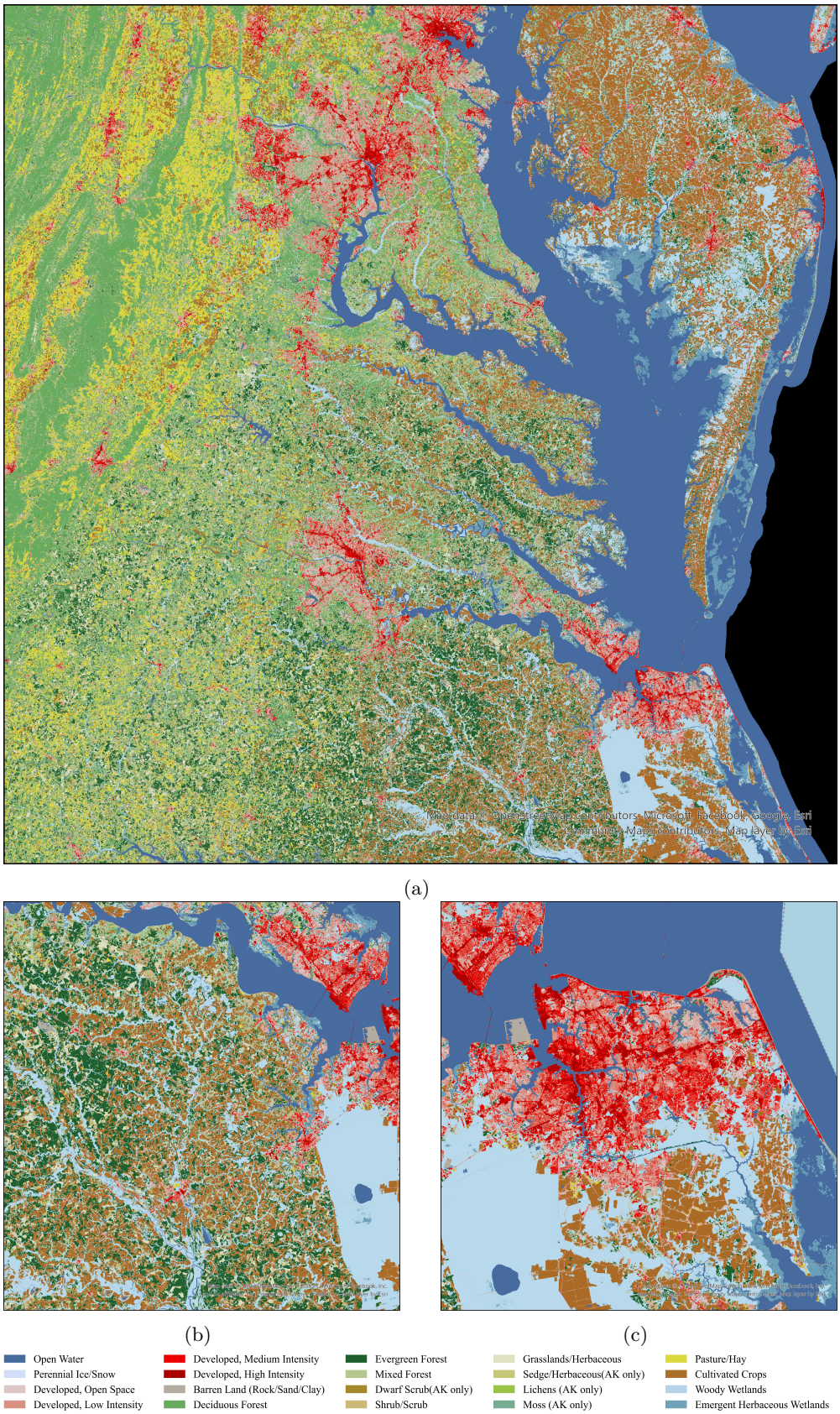

Supplementary Figure 7: Land cover integration for environmental vulnerability characterization using NLCD 2023 classification data. (a) Regional land cover patterns reveal heterogeneous environmental conditions affecting hurricane impact mechanisms, with detailed views of (b) Suffolk and (c) Chesapeake showing how forest coverage, urban development, and wetland proximity influence distribution infrastructure vulnerability.

The resulting geospatially-enhanced distribution networks, illustrated comprehensively in Supplementary Figure 8, provide the essential geographic foundation for high-resolution hurricane impact modeling described in the main text. These integrated datasets enable interdisciplinary collaboration between power systems engineers and climate scientists by providing a common framework for coupled simulations that accurately represent hurricane impact mechanisms across diverse geographic and environmental contexts. The detailed characterization of infrastructure-environment interactions supports the development of location-specific resilience strategies that account for local vulnerability factors, ultimately improving the accuracy and effectiveness of climate-informed grid hardening decisions.

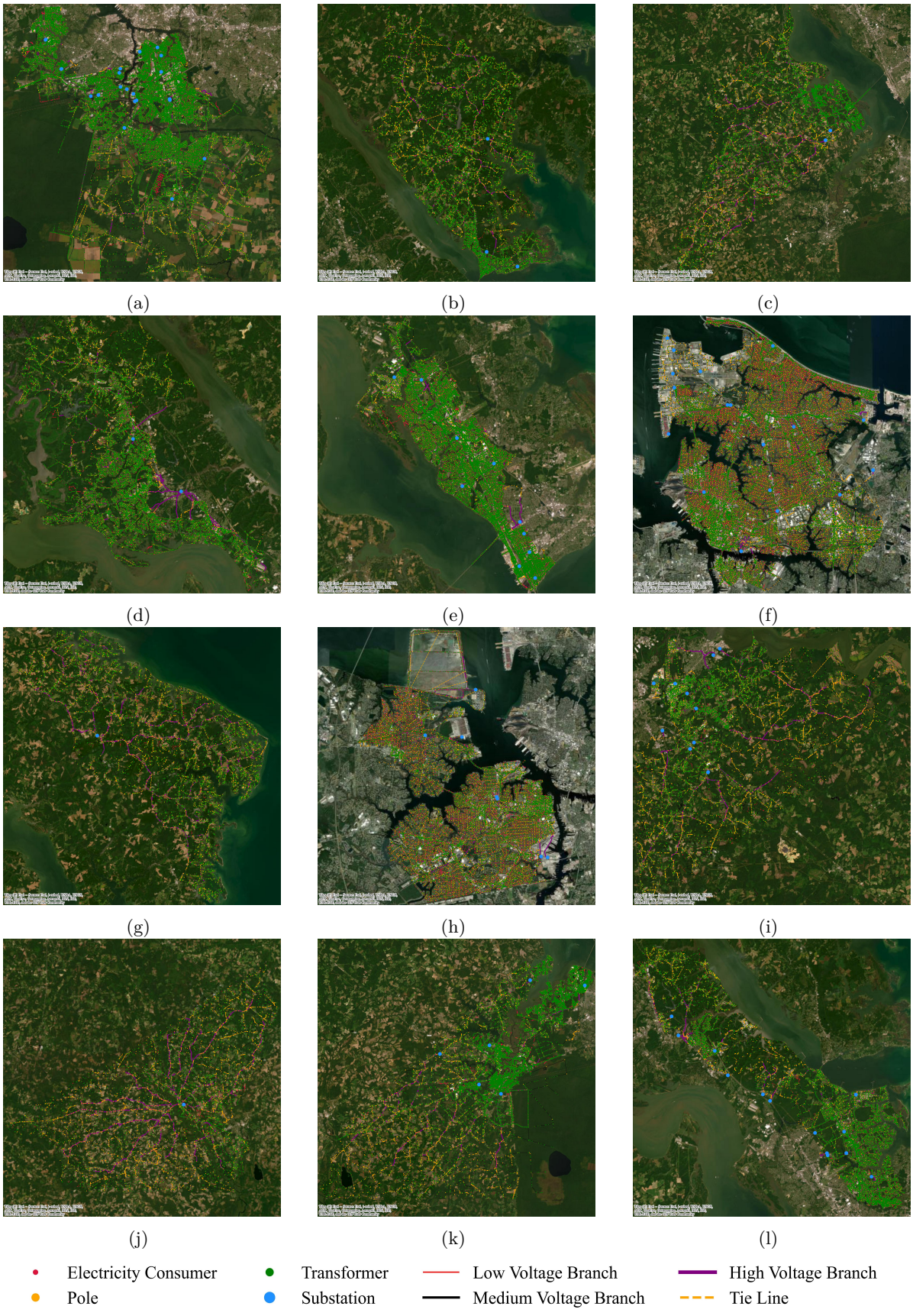

Supplementary Figure 8: Geospatially-enhanced distribution networks for comprehensive hurricane resilience modeling across Virginia coastal cities. (a) Chesapeake, (b) Gloucester, (c) Isle of Wight, (d) James City, (e) Newport News, (f) Norfolk, (g) Northumberland, (h) Portsmouth, (i) Prince George, (j) Southampton, (k) Suffolk, (l) York.

Supplementary Note 5: Comprehensive hurricane climatology and trajectory analysis for resilience assessment

Robust climate-informed resilience planning requires comprehensive analysis of historical hurricane activity to characterize the full range of potential impact scenarios facing coastal distribution infrastructure. The design of effective hurricane-resistant electrical systems depends fundamentally on understanding the meteorological diversity, seasonal patterns, and intensity distributions of tropical cyclones that have historically threatened or impacted the study region. We utilize the International Best Track Archive for Climate Stewardship (IBTrACS) database [8], which provides the most complete global collection of tropical cyclone best track data, to construct a representative ensemble of hurricane events spanning five decades of Atlantic basin activity that directly informs our resilience optimization framework.

Our comprehensive hurricane dataset encompasses 38 significant tropical cyclones that have impacted or threatened the Virginia coastal region between 1974 and 2024, as detailed in Supplementary Table **2**.

The selected storms represent critical benchmarks for infrastructure resilience assessment, ranging from catastrophic regional events such as Hurricane Hugo (1989) [9] and Hurricane Isabel (2003) [10] that caused widespread multi-state power outages affecting millions of customers, to more recent threats including Hurricane Florence (2018) [11] and Hurricane Helene (2024) [12] that demonstrated evolving patterns of hurricane behavior under changing climate conditions including slower forward speeds, increased rainfall rates, and enhanced storm surge potential.

Supplementary Table 2: Meteorological characteristics of historical hurricanes impacting Virginia coastal region (1974-2024), derived from IBTrACS best track data. Storm parameters include maximum sustained winds, minimum central pressure, and Saffir-Simpson classification at peak intensity, providing comprehensive climatological context for infrastructure vulnerability assessment and resilience planning scenarios.

Storm Name	Year	Date Range	Max Wind (mph)	Min Pressure (mbar)	Category
Helene [12]	2024	Sep 24 to Sep 29	140	939	H4
Debby [13]	2024	Aug 3 to Aug 11	80	979	H1
Ophelia [14]	2023	Sep 22 to Sep 25	70	981	TS
Nicole [15]	2022	Nov 7 to Nov 11	75	980	H1
Ian [16]	2022	Sep 23 to Oct 1	160	937	H5
Fred [17]	2021	Aug 11 to Aug 20	65	991	TS
Elsa [18]	2021	Jun 30 to Jul 10	75	991	H1
Wanda [19]	2021	Oct 25 to Nov 7	70	973	TS
Isaias [20]	2020	Jul 28 to Aug 5	80	986	H1
Zeta [21]	2020	Oct 24 to Oct 30	100	970	H3
Dorian [22]	2019	Aug 24 to Sep 10	185	910	H5
Michael [23]	2018	Oct 7 to Oct 16	160	919	H5
Florence [11]	2018	Aug 31 to Sep 18	150	937	H4
Cindy [24]	2017	Jun 20 to Jun 24	60	991	TS
Hermine [25]	2016	Aug 28 to Sep 8	80	981	H1
Colin [26]	2016	Jun 5 to Jun 8	50	1001	TS
Matthew [27]	2016	Sep 28 to Oct 10	165	934	H5
Sandy [28]	2012	Oct 22 to Nov 2	115	940	H3
Irene [29]	2011	Aug 21 to Aug 30	105	942	H3
Hanna [30]	2008	Aug 28 to Sep 8	70	977	TS
Ernesto [31]	2006	Aug 24 to Sep 4	70	995	TS
Cindy [32]	2005	Jul 5 to Jul 11	70	992	TS
Charley [33]	2004	Aug 9 to Aug 15	130	941	H4
Frances [34]	2004	Aug 24 to Sep 10	145	935	H4
Ivan [35]	2004	Aug 31 to Sep 24	145	910	H5
Isabel [10]	2003	Sep 6 to Sep 20	145	915	H5
Floyd [36]	1999	Sep 7 to Sep 19	135	921	H4
Dennis [37]	1999	Aug 24 to Sep 9	105	962	H2
Bonnie [38]	1998	Aug 19 to Aug 30	115	954	H3
Josephine [39]	1996	Oct 4 to Oct 13	70	981	TS
Bertha [40]	1996	Jul 5 to Jul 17	100	960	H3
Fran [41]	1996	Aug 23 to Sep 10	120	946	H3
Opal [42]	1995	Sep 27 to Oct 6	150	916	H4
Beryl [43]	1994	Aug 14 to Aug 19	60	999	TS
Hugo [9]	1989	Sep 10 to Sep 25	160	918	H5
Chris [44]	1988	Aug 21 to Aug 30	50	1005	TS
Charley [45]	1986	Aug 13 to Aug 30	70	990	TS
Gloria [46]	1985	Sep 16 to Oct 4	145	919	H4
David [47]	1979	Aug 25 to Sep 8	175	927	H5

To systematically evaluate how hurricane approach direction influences infrastructure vulnerability patterns, we analyze relative positioning between distribution networks and storm trajectories across multiple directional scenarios. Supplementary Figure **9**a and Figure **9**b demonstrates how approach angle fundamentally alters wind exposure patterns and damage potential for representative cities, with Suffolk and Chesapeake showing markedly different vulnerability profiles based on storm direction relative to local network topology and geographic features.

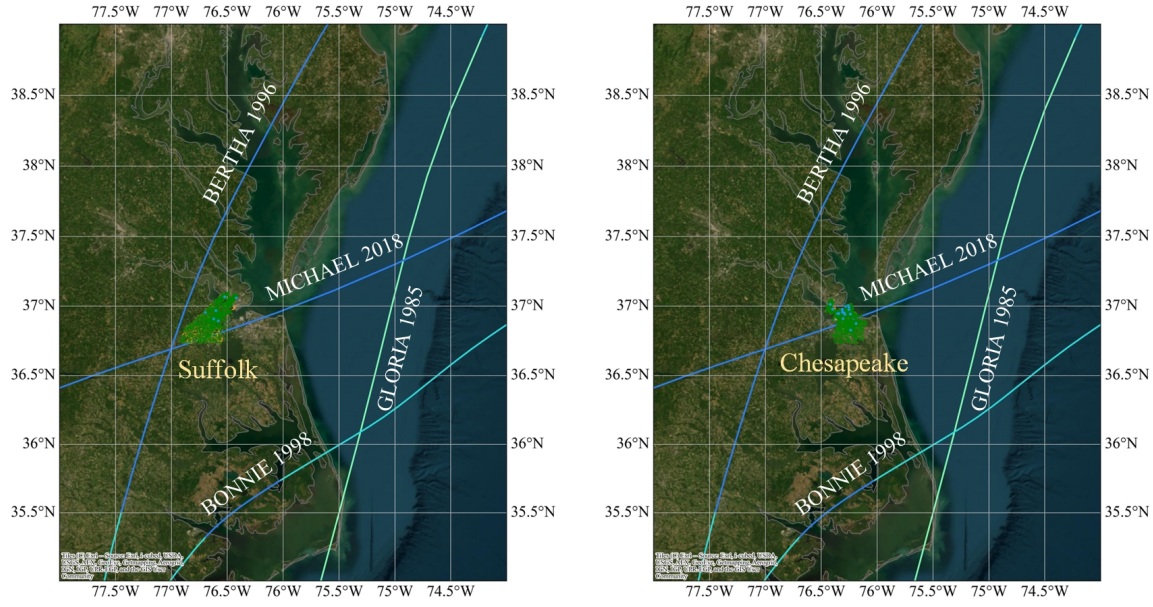

(a) (b)

Supplementary Figure 9: Directional hurricane approach scenarios for infrastructure vulnerability assessment. Analysis of relative positioning between distribution networks and hurricane trajectories demonstrates how approach angle influences wind exposure patterns and infrastructure damage potential, with examples from Suffolk (a) and Chesapeake (b) showing varied vulnerability profiles based on storm direction and local network topology.

The five-decade hurricane trajectory climatology presented in Supplementary Figure **10**a to **10**c reveals distinct regional exposure patterns that inform location-specific resilience strategies across Virginia's diverse geographic zones. Coastal cities like Williamsburg experience frequent direct hurricane impacts from storms following northward tracks along the Atlantic seaboard, while inland communities such as Galax encounter primarily weakened storms that have crossed the Appalachian Mountains, resulting in significantly different wind speed distributions and impact characteristics. Urban corridor locations like Fairfax exhibit intermediate exposure patterns, experiencing both direct coastal storms and inland-penetrating systems that create complex vulnerability profiles requiring nuanced resilience approaches.

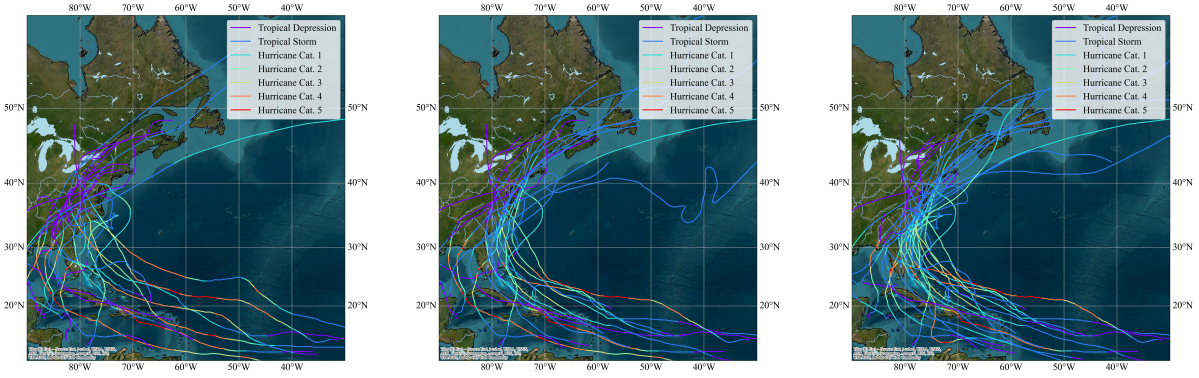

(a) (b) (c)

Supplementary Figure 10: Five-decade hurricane trajectory climatology for regional resilience planning across Virginia geographic zones (1974-2024). Historical storm tracks demonstrate diverse ranges of hurricane approaches, intensities, and seasonal patterns affecting regional infrastructure, providing essential climatological context for probabilistic risk assessment and long-term adaptation strategies. (a) Galax (b) Fairfax, and (c) Williamsburg.

Supplementary Note 6: Climate-adjusted hurricane intensity projections for infrastructure resilience planning

Comprehensive resilience assessment requires systematic accounting for the evolving characteristics of hurricane activity under anthropogenic climate change, as historical storm records alone may inadequately represent future threat conditions facing coastal electrical infrastructure during their operational lifetimes. Climate change is projected to fundamentally alter hurricane characteristics through multiple physical mechanisms, including enhanced upper-ocean heat content that fuels storm intensification, modified atmospheric circulation patterns that affect storm tracks, and increased thermodynamic instability that promotes rapid intensification processes. We implement systematic climate adjustments to our historical hurricane dataset to ensure consistency with projected mid-century climate conditions, enabling forward-looking resilience planning that accounts for anticipated changes in storm intensity distributions and frequency patterns that will affect infrastructure vulnerability throughout the 2050 planning horizon.

Our climate correction methodology follows the dynamical downscaling approach established by Knutson et al.[48], which employs high-resolution atmospheric models to simulate tropical cyclone activity under observed sea surface temperature conditions and CMIP5 global climate model projections. This technique captures complex interactions between large-scale climate forcing and mesoscale hurricane dynamics, including the effects of ocean warming on storm energy availability, atmospheric circulation changes that influence steering patterns, and thermodynamic environment modifications that alter storm development and intensification processes. The methodology employs ensemble statistics from multiple global climate models to reduce uncertainty and provide robust projections of future hurricane activity across different emission scenarios and climate sensitivities.

We apply Representative Concentration Pathway 4.5 (RCP4.5) as our reference climate scenario, representing a moderate greenhouse gas emission trajectory consistent with current international climate policy commitments and recent emission trends. This scenario projects atmospheric CO_2 concentrations reaching approximately 540 ppm by 2050, resulting in global warming of 1.5-2.0above pre-industrial levels with corresponding impacts on tropical cyclone activity. The climate adjustment factors are derived from ensemble statistics comparing late twenty-first century projections (2081-2100) with present-day climatology (1982-2005), with linear interpolation applied to generate corrections appropriate for our 2050 planning horizon. This temporal interpolation approach ensures that infrastructure investments evaluated using our framework reflect climate conditions expected during their operational lifetime rather than current or end-of-century extremes.

The climate adjustments capture several key projected changes in North Atlantic hurricane activity that directly affect infrastructure vulnerability assessment, as quantified in Supplementary Table **3**. The most significant finding for infrastructure planning is the projected 42.1% increase in intense hurricanes (Categories 4-5) in the North Atlantic basin, despite an overall 17.5% decrease in total hurricane frequency. This shift toward more intense storms creates a fundamental change in the risk profile facing electrical distribution infrastructure, as Categories 4-5 hurricanes generate wind speeds exceeding 130 mph that substantially increase failure probabilities for overhead power lines, distribution transformers, and utility poles. Additionally, maximum wind speeds for all hurricane categories are projected to increase by 4.5% in the North Atlantic, translating to enhanced wind loading on infrastructure components even for storms of nominally equivalent intensity categories.

The climate-adjusted hurricane characteristics enable more accurate assessment of future infrastructure vulnerability by incorporating projected changes in storm intensity distributions rather than assuming stationary climate conditions. These adjustments ensure that our resilience optimization framework accounts for the evolving hurricane threat environment, supporting the development of adaptation strategies that maintain effectiveness under anticipated climate change impacts. The resulting climate-informed projections provide essential input for the risk-calibrated planning strategies described in the main text, enabling utilities and regulators to make infrastructure investment decisions based on scientifically grounded assessments of future hurricane risk rather than historical precedent alone.

Supplementary Table 3: Projected changes in North Atlantic hurricane characteristics under RCP4.5 climate scenario for infrastructure resilience planning. Quantitative projections of tropical cyclone activity changes (percent deviation from 1982-2005 baseline) derived from CMIP5 multi-model ensemble downscaling experiments following Knutson et al. methodology. Future climate conditions represent averaged projections for late twenty-first century with linear interpolation to 2050 planning horizon, providing empirical basis for climate-informed hurricane intensity corrections applied to historical storm database for infrastructure vulnerability assessment.

Hurricane Characteristic	**Global Change (%)**	**North Atlantic Change (%)**
Total tropical cyclones (Cat 0–5)	-16.4^{**}	-9.4
All hurricanes (Cat 1–5)	-16.6^{**}	-17.5
Major hurricanes (Cat 3–5)	$+1.8$	$+2.7$
Intense hurricanes (Cat 4–5)	$+28.3^{**}$	$+42.1$
Extreme hurricanes (wind >65 m/s)	$+59.3^{*}$	$+125.0$
Accumulated cyclone energy (ACE)	-13.1	-9.7
Power dissipation index (PDI)	-9.7^{**}	-3.1
Tropical storm max winds (m/s)	$+3.6^{**}$	$+0.4$
Hurricane max winds (m/s)	$+4.1^{**}$	$+4.5$
Cat 4–5 storm duration (days)	$+34.5^{**}$	$+175.4$
Precipitation intensification		
All tropical cyclones rainfall	$+14.3^{**}$	$+17.3^{**}$
Hurricane rainfall (Cat 1–5)	$+13.4^{**}$	$+20.5^{**}$
Major hurricane rainfall (Cat 3–5)	$+8.8^{**}$	$+14.0^{*}$
Intense hurricane rainfall (Cat 4–5)	$+7.7^{**}$	$+9.4$
Sea surface temperature increase	+1.546°C	+1.685°C

Statistical significance: ** $p < 0.01$, * $p < 0.05$ Positive values indicate increases; negative values indicate decreases

Supplementary Note 7: Terrain-adjusted hurricane wind field modeling for infrastructure vulnerability assessment

Accurate characterization of hurricane wind exposure requires sophisticated treatment of local terrain effects, as topographic features and land surface characteristics significantly modify the hurricane boundary layer structure and resulting wind speeds experienced by distribution infrastructure. We implement a comprehensive wind field correction methodology that accounts for both elevation-dependent atmospheric dynamics and land cover-induced surface roughness effects to provide realistic estimates of infrastructure wind loading during hurricane events.

Our approach integrates high-resolution digital elevation models with detailed land cover classifications to capture the complex interactions between hurricane winds and the heterogeneous coastal landscape. The fundamental physics governing wind speed variation with height above ground level follows the logarithmic wind profile relationship, which describes how atmospheric boundary layer turbulence modifies wind speeds based on surface roughness characteristics and measurement elevation.

The terrain-adjusted wind speed calculation employs the standard meteorological wind profile formulation [49]:

$$V_{3s}^{H,\text{land}}(r) = V_{3s}^{G,\text{land}}(r)\frac{\ln(H/z_0)}{\ln(z_G/z_0)} \tag{17}$$

where $V_{3s}^{H,\text{land}}(r)$ represents the 3-second gust wind speed at infrastructure height H above ground level in the land environment at radial distance r from the hurricane center, $V_{3s}^{G,\text{land}}(r)$ denotes the reference gust speed at the standard meteorological measurement height z_G (typically 10 meters), H corresponds to the specific elevation of distribution infrastructure components (utility poles, transmission towers), z_0 represents the aerodynamic surface roughness length characteristic of the local land cover type, and z_G is the reference measurement height for the baseline wind speed data.

The surface roughness parameter z_0 varies significantly across land cover types, ranging from approximately 0.0002 m for open water surfaces to 0.5-2.0 m for dense urban environments and mature forest canopies. We assign roughness values to each network component based on the underlying NLCD land cover classification, ensuring that wind speed estimates reflect the local aerodynamic environment experienced by infrastructure elements. This approach captures the substantial wind speed reductions that occur in forested areas compared to open terrain, as well as the enhanced turbulence and directional variability characteristic of urban environments.

Supplementary Note 8: Spatio-temporal hurricane damage modeling for dynamic infrastructure failure assessment

Comprehensive hurricane resilience assessment requires sophisticated modeling of the temporal evolution of infrastructure failure risk as storms progress across distribution networks. We develop a high-fidelity spatio-temporal failure simulation framework that captures the dynamic interaction between hurricane wind fields and distribution infrastructure, enabling quantitative assessment of outage propagation patterns and identification of temporally critical vulnerability windows for emergency response planning.

Our methodology integrates the physically-based hurricane wind field model [50] with empirically-derived infrastructure vulnerability functions to simulate realistic failure scenarios throughout hurricane passage. For each network component, we establish the shortest distance to the hurricane eye using geometric optimization algorithms: point-to-point calculations for discrete infrastructure elements (poles, transformers, substations) and line-to-point distance minimization using Heron's formula for distribution feeders. These distances provide the spatial coordinates necessary for wind speed estimation using the wind field model.

The failure probability assessment distinguishes between two primary hurricane damage mechanisms affecting overhead distribution infrastructure. Direct wind damage occurs when sustained winds or gusts exceed the mechanical design limits of poles, conductors, or support structures, typically manifesting as structural failure or equipment displacement. Indirect wind damage results from wind-driven projectiles, primarily fallen trees and vegetation debris, which cause secondary failures by impacting power lines or creating fault conditions that trigger protective equipment operation.

We employ empirically-calibrated lognormal vulnerability curves derived from extensive historical outage analysis to quantify component failure probabilities as functions of local wind speed exposure:

$$\mathsf{P}(\text{failure} \mid w) = \Phi\left[\frac{1}{\beta}\left(\ln w - \lambda\right)\right], \tag{18}$$

where $\mathsf{P}(\text{failure} \mid w)$ represents the probability of component failure given wind speed w, $\Phi(\cdot)$ denotes the standard normal cumulative distribution function, $\beta = 0.2061$ is the lognormal scale parameter calibrated from regional outage data, and $\lambda = 4.4057$ is the location parameter that determines the median failure wind speed [51]. This probabilistic formulation captures the inherent uncertainty in infrastructure performance under extreme wind loading while providing quantitative estimates suitable for risk-informed decision making.

The comprehensive modeling framework reveals pronounced spatial heterogeneity in hurricane-induced outage risk across Virginia coastal distribution networks, as demonstrated in Supplementary Figure 11 for Hurricane Gloria (1985). Peak and minimum line outage probabilities consistently exhibit differences exceeding 60% across all study cities, illustrating the critical importance of high-resolution meteorological modeling for capturing localized vulnerability patterns that would be overlooked by uniform or simplified wind field assumptions. The temporal evolution of outage risk patterns, shown in Supplementary Figures 12 and 13, reveals how local topography, land cover characteristics, and network topology influence the spatio-temporal progression of hurricane vulnerability. These dynamic simulations enable identification of peak risk periods and optimal timing for emergency response deployment, supporting the development of location-specific emergency management strategies tailored to regional infrastructure characteristics and storm progression patterns.

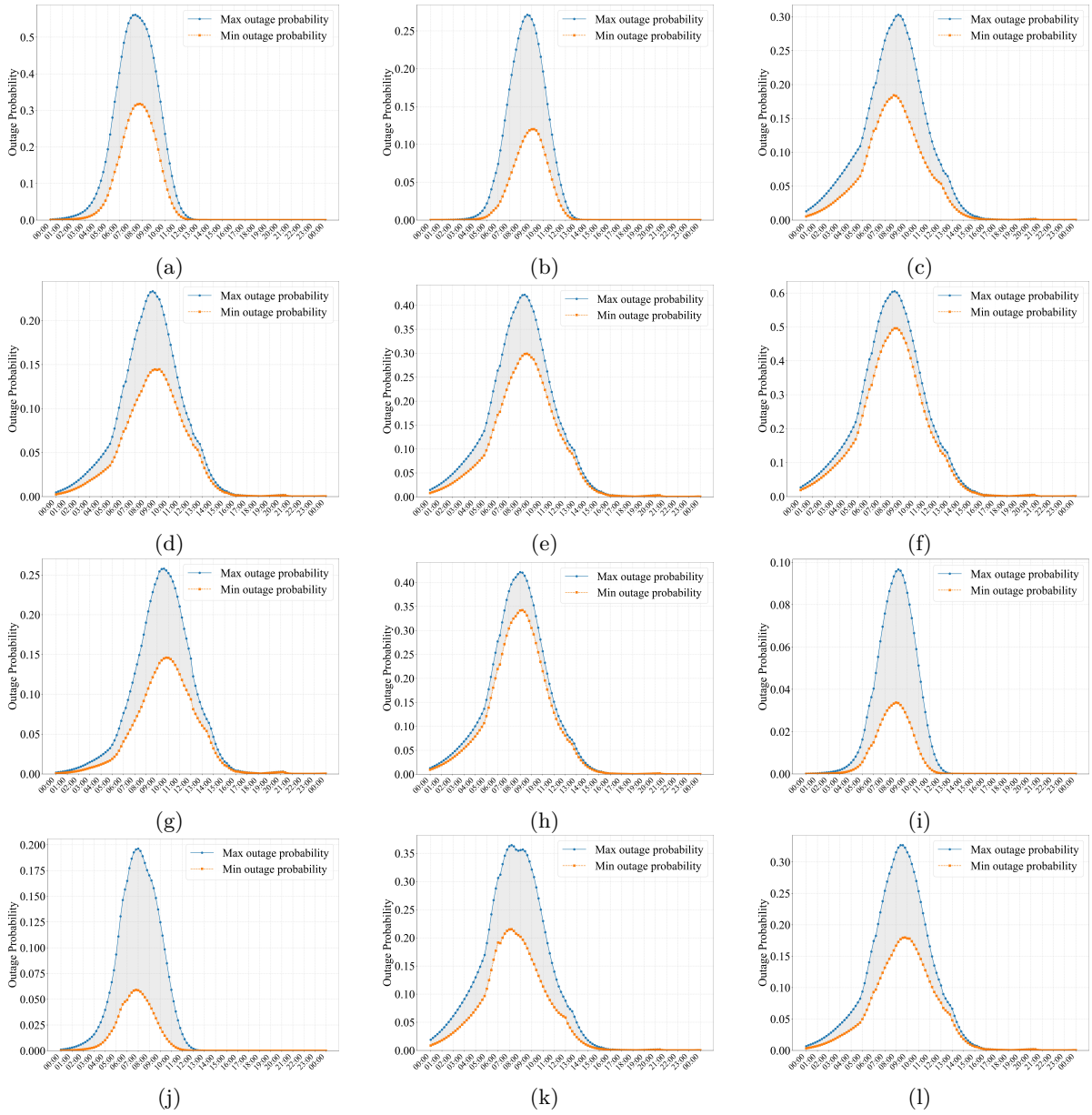

Supplementary Figure 11: Regional heterogeneity in hurricane-induced outage risk across Virginia coastal distribution networks during Hurricane Gloria (1985). Peak and minimum line outage probabilities reveal pronounced spatial variability, with maximum-minimum probability differences exceeding 60% across all study cities, demonstrating the critical importance of high-resolution meteorological modeling for capturing localized vulnerability patterns essential for targeted resilience planning. (a) Chesapeake, (b) Gloucester, (c) Isle of Wight, (d) James City, (e) Newport News, (f) Norfolk, (g) Northumberland, (h) Portsmouth, (i) Prince George, (j) Southampton, (k) Suffolk, (l) York.

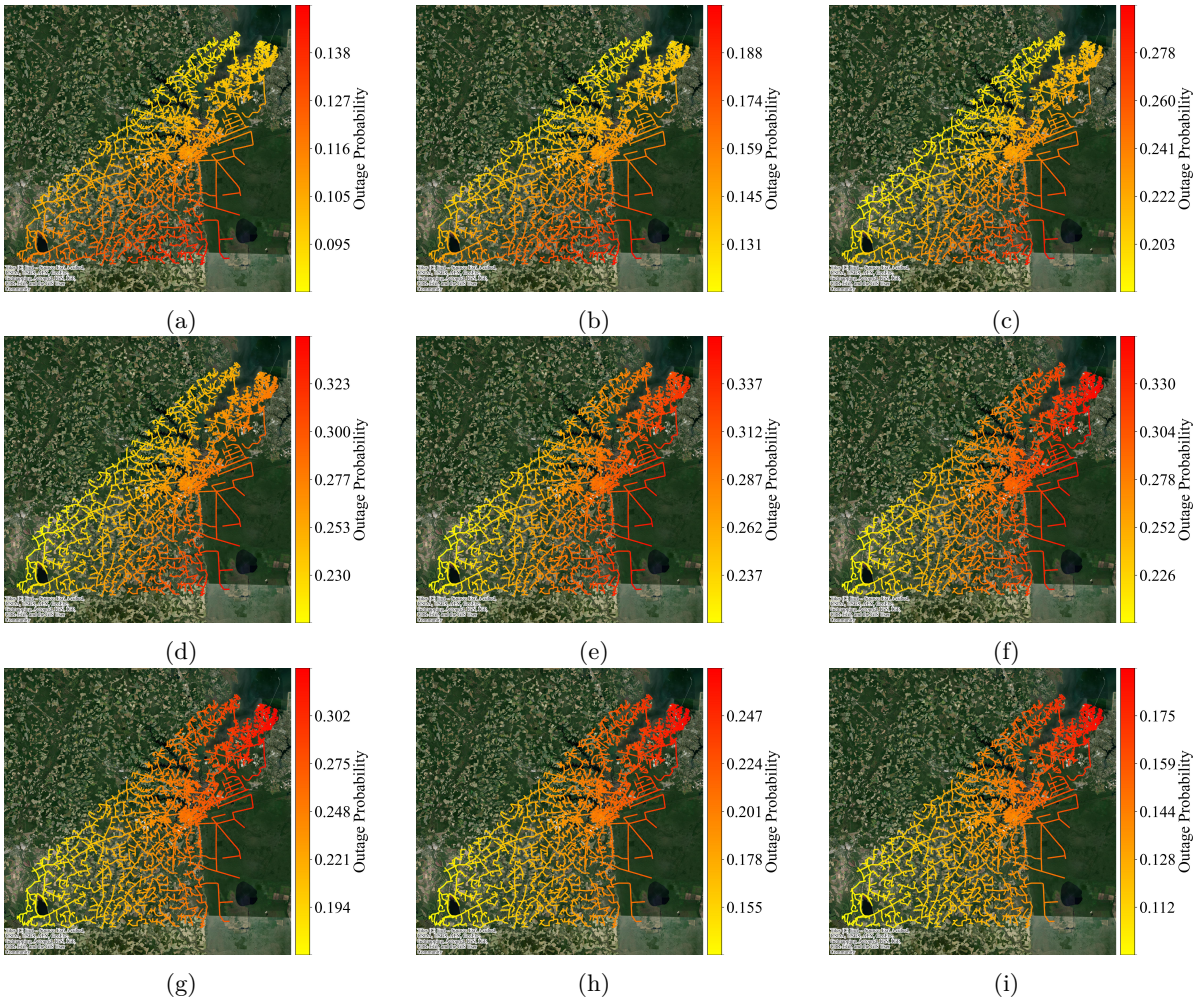

Supplementary Figure 12: Temporal evolution of hurricane-induced outage risk in Suffolk distribution network during Hurricane Gloria (1985) passage. Nine-panel time series demonstrates the dynamic progression of line outage probabilities as the hurricane approaches, makes closest approach, and departs, revealing spatially heterogeneous vulnerability patterns that evolve throughout the storm event and inform optimal timing for emergency response deployment.

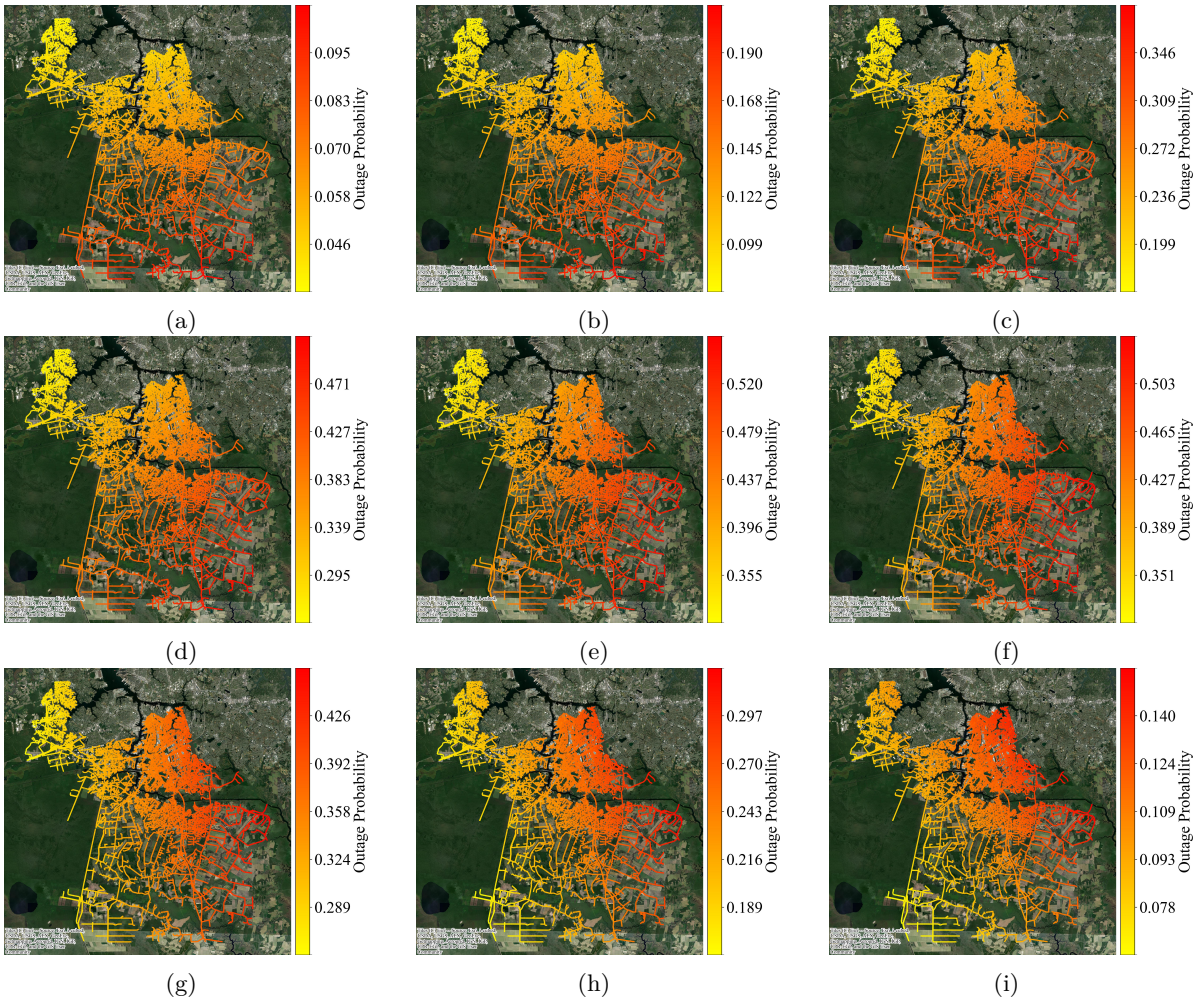

Supplementary Figure 13: Temporal evolution of hurricane-induced outage risk in Chesapeake distribution network during Hurricane Gloria (1985) passage. Comparative analysis with Suffolk demonstrates how local topography, land cover, and network topology influence the spatio-temporal patterns of hurricane vulnerability, enabling development of location-specific emergency response strategies tailored to regional infrastructure characteristics.

Supplementary Note 9: Probabilistic outage scenario generation using hazard resistance-based spatio-temporal simulation

Accurate simulation of hurricane-induced distribution network failures requires sophisticated Monte Carlo methodologies that capture the stochastic nature of infrastructure performance while avoiding systematic biases inherent in traditional sampling approaches. Conventional Sequential Monte Carlo (SMC) simulation methods sample component failure probabilities at discrete time intervals throughout hurricane passage, but this approach suffers from temporal accumulation bias that systematically overestimates outage frequency when applied to high-resolution meteorological datasets.

The fundamental limitation of standard SMC approaches lies in their treatment of failure probability as a time-varying random process. When failure probabilities are repeatedly sampled at fine temporal resolution, the cumulative probability of component failure approaches unity even under moderate wind conditions, leading to unrealistic outage scenarios that exceed empirically observed failure rates. This temporal bias becomes particularly problematic when integrating high-resolution climate models with infrastructure simulation, as the increased sampling frequency exacerbates the overestimation effect and compromises the reliability of resilience assessments.

To address these methodological limitations, we implement the Hazard Resistance-Based Spatio-temporal Risk Analysis (HRSRA) framework[51], which transforms the traditional time-varying fail-

ure probability formulation into a time-invariant critical resistance approach. This transformation preserves the fundamental physics of component vulnerability while eliminating temporal accumulation bias through a mathematically rigorous reformulation of the failure assessment process.

The HRSRA methodology assigns each distribution component a critical wind resistance threshold R_i^W that remains constant throughout the hurricane simulation period. Component failure occurs when the local wind speed exceeds this resistance threshold, but the threshold itself does not change with time. The critical resistance values are generated using inverse transform sampling from the component vulnerability distribution:

$$R_i^W = F_{RW}^{-1}(r_i) = \exp\left(\lambda + \beta \cdot \Phi^{-1}(r_i)\right), \quad i \in \mathcal{I}_f \tag{19}$$

where $F_{RW}^{-1}(\cdot)$ represents the inverse cumulative distribution function of the critical resistance, $r_i \sim U(0,1)$ is a uniformly distributed random sample, λ and β are the lognormal distribution parameters from the vulnerability function, $\Phi^{-1}(\cdot)$ denotes the inverse standard normal cumulative distribution function, and $\mathcal{I}_f$ represents the set of distribution feeders in the network.

This transformation maintains mathematical equivalence with the original vulnerability formulation while eliminating temporal bias: the cumulative distribution function of critical resistance satisfies $F_{RW}(w) = P(R_i^W \leq w) = P(\text{failure}|w)$, ensuring that the probability of component resistance being less than a given wind speed equals the failure probability at that wind speed from the original fragility function.

The HRSRA approach enables unbiased high-resolution spatio-temporal simulation by mapping the failure probability sample space to a critical resistance sample space with time-invariant properties. Each Monte Carlo realization assigns fixed resistance thresholds to all network components, and these thresholds determine failure states through direct comparison with time-varying wind speeds rather than repeated probability sampling. This methodology eliminates accumulation bias while preserving the stochastic nature of infrastructure performance, enabling reliable integration of high-resolution meteorological models with infrastructure vulnerability assessment.

We perform 1,000 independent Monte Carlo simulations for each hurricane scenario, generating comprehensive probabilistic outage datasets that capture the uncertainty in infrastructure performance while maintaining statistical consistency with empirically observed failure patterns. This extensive simulation ensemble provides robust statistical foundations for resilience metric calculation and uncertainty quantification in climate-informed planning applications.

Supplementary Note 10: Stratified Monte Carlo scenario reduction for computationally efficient hurricane resilience assessment

Comprehensive hurricane resilience analysis requires evaluation of thousands of potential failure scenarios to capture the full statistical range of infrastructure vulnerability patterns, yet computational constraints necessitate strategic scenario reduction methodologies to enable practical implementation in operational planning environments. Traditional Monte Carlo simulation approaches generate extensive failure scenario ensembles that, while statistically comprehensive, exceed the computational limits of optimization-based resilience assessment frameworks when applied to large-scale urban power distribution networks. We develop a stratified sampling methodology that systematically identifies representative failure scenarios while preserving the essential statistical characteristics of the complete Monte Carlo ensemble, ensuring that computationally tractable scenario sets maintain accuracy for critical infrastructure assessment and emergency response optimization without sacrificing statistical rigor or decision-making quality.

Traditional random sampling approaches for scenario reduction suffer from potential loss of optimization accuracy, particularly when dealing with low-probability, high-consequence failure events that are crucial for resilience planning but may be underrepresented in small sample sets due to their statistical rarity. Our stratified reduction methodology addresses this fundamental limitation by implementing a convergence-based selection process that ensures representative scenarios capture the essential statistical properties of the complete failure distribution while maintaining computational tractability for real-time emergency response analysis. The approach recognizes that effective scenario reduction must balance computational efficiency with preservation of critical tail events that dominate resilience planning decisions.

The stratified scenario reduction algorithm employs an iterative convergence approach for each hurricane event h in our comprehensive storm database. Beginning with the complete set of 1,000 HRSRA-

generated failure scenarios, we progressively evaluate subsets of increasing size n until the weighted load shedding metric converges to a statistically stable value. For each scenario s within the evaluation subset, we apply the complete emergency response optimization model to calculate the weighted critical load loss $P_{h,s}^{\text{shed}}$ under optimal network reconfiguration, microgrid formation, and load curtailment strategies. The convergence criterion ensures statistical stability by requiring that the average weighted load loss difference between ten consecutive iterations remains below 0.01 MW, indicating that additional scenarios do not materially alter the expected system performance metrics. Once convergence is achieved, we select the specific outage scenario set Γ_s whose load shedding value most closely approximates the converged ensemble average as the representative scenario Γ_h for hurricane h, ensuring that the selected scenario reflects the central tendency of the failure distribution while capturing realistic spatial and temporal infrastructure damage patterns.

The emergency response optimization model integrated within the scenario reduction framework simultaneously addresses network reconfiguration, microgrid formation, and load curtailment decisions to minimize critical load interruption under post-hurricane conditions. This optimization framework considers damaged line conditions as input constraints derived from the HRSRA simulation results and determines optimal operational strategies that maximize service restoration capabilities. The mathematical formulation encompasses the complete set of operational constraints necessary for feasible emergency operations and subject to comprehensive operational constraints including power flow balance, reactive power balance, generation capacity limits, transmission capacity constraints, outage-induced operational restrictions, load shedding bounds, network connectivity requirements, voltage regulation, and radiality maintenance constraints.

$$\min \sum_{i \in \mathcal{N}} (1-\delta_i)\, \omega_i\, P_i^{\text{shed}} \tag{20}$$

$$\sum_{\{j \mid j \in \mathcal{RL}_i^{up}\}} P_{ij} - \sum_{\{j \mid j \in \mathcal{RL}_i^{dn}\}} P_{ij} + \sum_{\{j \mid j<i,\,(i,j) \in \mathcal{TL}\}} P_{ij} - \sum_{\{j \mid i<j,\,(i,j) \in \mathcal{TL}\}} P_{ij} = \left(P_i^L - P_i^{\text{shed}}\right) - P_i^G,\ \forall i \in \mathcal{N} \tag{21}$$

$$\sum_{\{j \mid j \in \mathcal{RL}_i^{up}\}} Q_{ij} - \sum_{\{j \mid j \in \mathcal{RL}_i^{dn}\}} Q_{ij} + \sum_{\{j \mid j<i,\,(i,j) \in \mathcal{TL}\}} Q_{ij} - \sum_{\{j \mid i<j,\,(i,j) \in \mathcal{TL}\}} Q_{ij} = \left(Q_i^L - Q_i^{\text{shed}}\right) - Q_i^G,\ \forall i \in \mathcal{N} \tag{22}$$

$$0 \le P_i^G \le \overline{P}_i^G, \quad 0 \le Q_i^G \le \overline{Q}_i^G,\ \forall i \in \mathcal{S} \cup \mathcal{DG} \tag{23}$$

$$-\,u_{ij}\,\overline{P}_{ij} \;\le\; P_{ij} \;\le\; u_{ij}\,\overline{P}_{ij}, \quad -u_{ij}\,\overline{Q}_{ij} \;\le\; Q_{ij} \;\le\; u_{ij}\,\overline{Q}_{ij},\ \forall (i,j) \in \mathcal{L} \tag{24}$$

$$u_{ij} \le 1 - \tau_{ij}, \quad \forall \tau_{ij} \in \Gamma,\ (i,j) \in \mathcal{L} \tag{25}$$

$$(1-\delta_i)\, P_i^L \le P_i^{\text{shed}} \le P_i^L, \quad \forall i \in \mathcal{N} \tag{26}$$

$$\delta_i \le h_i, \quad \forall i \in \mathcal{N} \tag{27}$$

$$\frac{\sum_{j \in \mathcal{RL}_i^{dn}} h_j\, u_{ij} + \sum_{j \in \mathcal{RL}_i^{up}} h_j\, u_{ij}}{|\mathcal{L}_i|} \;\le\; h_i \;\le\; \sum_{j \in \mathcal{RL}_i^{dn}} h_j\, u_{ij} + \sum_{j \in \mathcal{RL}_i^{up}} h_j\, u_{ji},\ \forall i \in \mathcal{N} \setminus (\mathcal{S} \cup \mathcal{DG}) \tag{28}$$

$$-\,M\,(1-u_{ij}) + \frac{r_{ij}P_{ij} + x_{ij}Q_{ij}}{V_0} \;\le\; V_i - V_j \;\le\; M\,(1-u_{ij}) + \frac{r_{ij}P_{ij} + x_{ij}Q_{ij}}{V_0},\ \forall (i,j) \in \mathcal{L} \tag{29}$$

$$\underline{V}_i \le V_i \le \overline{V}_i, \quad \forall i \in \mathcal{N} \tag{30}$$

$$\xi_{ij}^{+} + \xi_{ij}^{-} = u_{ij}, \quad \forall (i,j) \in \mathcal{L} \tag{31}$$

$$\sum_{j \in \mathcal{L}_i^{up}} \xi_{ij}^{+} + \sum_{j \in \mathcal{L}_i^{dn}} \xi_{ij}^{-} \le \lambda_{\max},\ \forall i \in \mathcal{N} \setminus \mathcal{S} \tag{32}$$

$$\sum_{i \in \mathcal{S}} \Big(\sum_{j \in \mathcal{L}_i^{up}} \xi_{ij}^{+} + \sum_{j \in \mathcal{L}_i^{dn}} \xi_{ij}^{-} \Big) \le \lambda_{\max} \tag{33}$$

where δ_i represents the binary service restoration status for load node i (1 if served, 0 if shed), ω_i denotes the criticality weight for load i based on infrastructure classification, P_i^{shed} represents the active power shed at node i in MW, $\mathcal{N}$ is the set of all network nodes, P_{ij} and Q_{ij} represent active and reactive power flows on line (i, j) respectively, $\mathcal{RL}_i^{up}$ and $\mathcal{RL}_i^{dn}$ denote the sets of upstream and downstream radial lines connected to node i, $\mathcal{TL}$ represents the set of tie lines for network reconfiguration, P_i^L and Q_i^L are the active and reactive power demands at node i, P_i^G and Q_i^G represent active and reactive power generation at node i, $\mathcal{S}$ and $\mathcal{DG}$ denote the sets of substation and distributed generation nodes respectively, u_{ij} is the binary line switching variable (1 if line is closed, 0 if open), τ_{ij} represents the binary outage status from scenario Γ (1 if line is damaged, 0 if intact), $\overline{P}_{ij}$ and $\overline{Q}_{ij}$ are the active and reactive power capacity limits for line (i, j), h_i represents the binary connectivity indicator for node i, V_i denotes the voltage magnitude at node i, r_{ij} and x_{ij} are the resistance and reactance of line (i, j), V_0 is the reference voltage magnitude, M is a sufficiently large constant for big-M constraints, ξ_{ij}^+ and ξ_{ij}^- are auxiliary variables for radiality enforcement [52], and $\lambda_{\max}$ represents the maximum allowable degree for maintaining radial network operation.

The computational efficiency demonstration using Hurricane Michael (2018) across representative Virginia distribution networks, presented in Supplementary Figure 14, validates the consistent performance of our stratified reduction methodology. Convergence analysis reveals that weighted critical load loss metrics stabilize rapidly across diverse network topologies, with all systems achieving statistical convergence well within the 1,000-iteration computational budget. The results demonstrate robust methodology performance across inland Galax, Fairfax, and Williamsburg, confirming the approach's broad applicability to heterogeneous infrastructure characteristics and geographical conditions essential for comprehensive regional resilience planning. This computational efficiency enables practical deployment of the methodology in operational emergency management applications while maintaining the statistical rigor necessary for evidence-based resilience investment decisions.

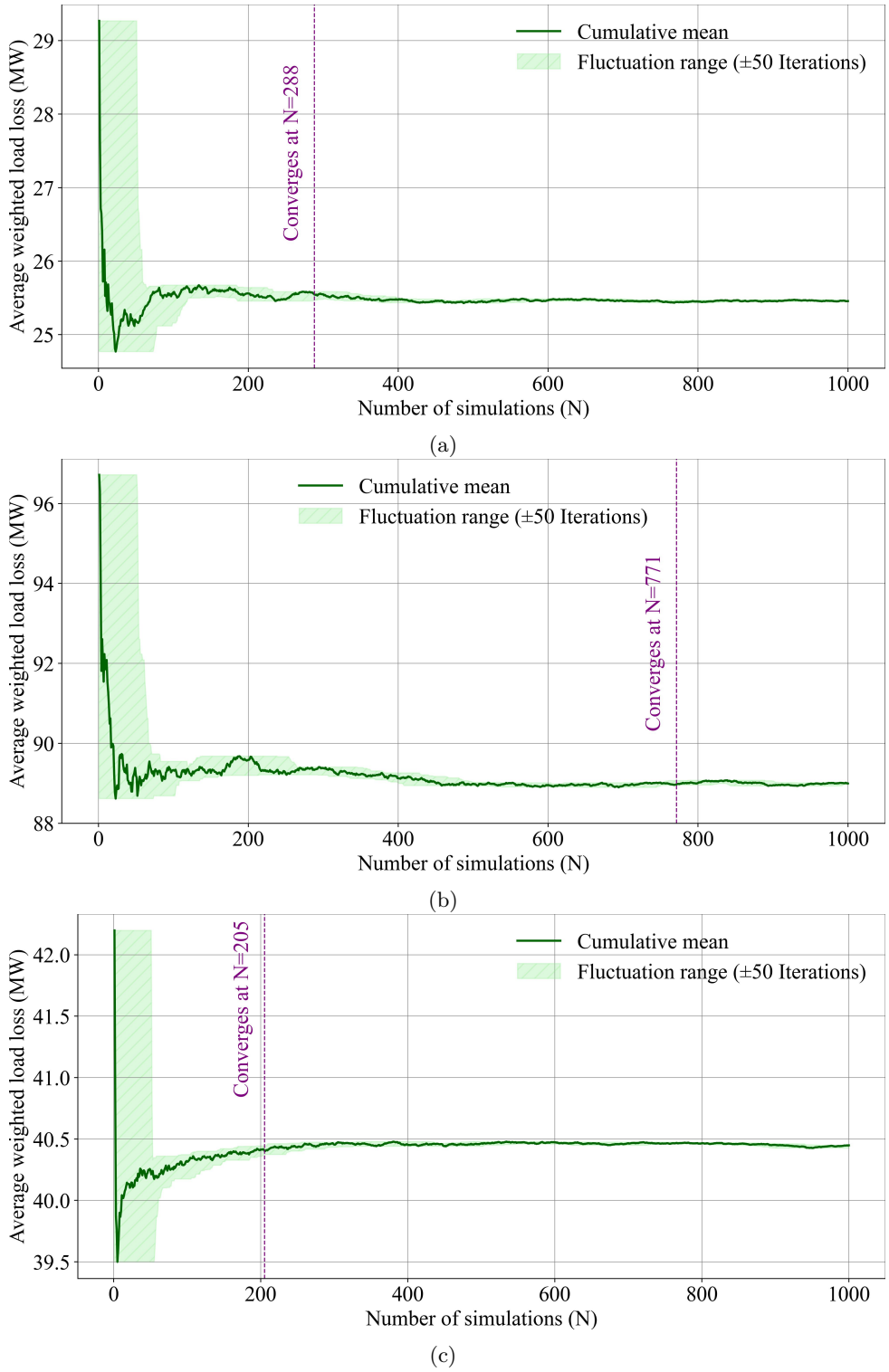

Supplementary Figure 14: Computational convergence demonstration of stratified scenario reduction methodology for Hurricane Michael (2018) across representative Virginia distribution networks with diverse topological and geographical characteristics. Convergence analysis demonstrates that weighted critical load loss metrics achieve statistical stability within 1,000 iterations across all network types, validating computational efficiency for operational emergency management applications. Results demonstrate consistent methodology performance across (a) Galax, (b) Fairfax, and (c) Williamsburg, validating the approach's applicability to heterogeneous infrastructure characteristics and geographical conditions essential for regional resilience planning.

Supplementary Note 11: Integrated infrastructure hardening and distributed generation planning for hurricane resilience optimization

Strategic resilience enhancement of distribution networks requires systematic integration of proactive infrastructure hardening with distributed generation deployment to minimize hurricane-induced service disruptions while optimizing limited capital investment resources. We develop a comprehensive planning optimization framework that simultaneously determines optimal locations for underground line conversion, distributed generator placement and sizing, and emergency network reconfiguration strategies to maximize system performance under hurricane conditions.

Our methodology enables comparative assessment of resilience investment strategies across three distinct wind field modeling approaches: uniform wind fields that assume spatially homogeneous conditions, static wind fields that capture spatial heterogeneity without temporal evolution, and our high-spatio-temporal-resolution (HSTR) dynamic wind field model that represents the complete four-dimensional hurricane impact. This comparative framework quantifies the value of enhanced meteorological modeling for infrastructure investment decision-making, demonstrating how improved wind field characterization influences optimal hardening strategies and resilience outcomes.

The integrated planning model addresses the complex interdependencies between infrastructure hardening decisions, distributed generation deployment, and operational flexibility under extreme weather conditions. Given representative failure scenarios Γ_h derived from scenario reduction analysis for hurricane h, the optimization framework determines the resilience investment portfolio $\mathbf{R}$ that minimizes expected critical load loss while respecting capital and operational constraints.

The decision variable set encompasses distributed generation placement indicators c_i, generator capacity allocations β_i, line hardening selections z_{ij}, and emergency operational variables including switch state u_{ij} and load curtailment decisions δ_i. The planning framework incorporates realistic resource constraints: maximum DG unit deployment $C_{\max} = 10$ units per network, total DG penetration limit $\theta_{\max}$, and line hardening budget $Z_{\max}$ sufficient for 30% underground conversion of existing overhead infrastructure.

The multi-objective optimization formulation minimizes weighted critical load interruption:

$$\min \sum_{i\in\mathcal{N}} (1-\delta_i)\,\omega_i\,P_i^{\text{shed}} \tag{34}$$

$$\sum_{i\in\mathcal{N}} c_i\beta_i \le \theta_{\max} \tag{35}$$

$$\sum_{i\in\mathcal{N}} c_i \le C_{\max} \tag{36}$$

$$\sum_{(i,j)\in\mathcal{L}} z_{ij} \le Z_{\max} \tag{37}$$

$$0 \;\le\; P_i^G \;\le\; c_i\overline{P}_i^G, \quad 0 \;\le\; Q_i^G \;\le\; c_i\overline{Q}_i^G, \quad \forall i\in\mathcal{N} \tag{38}$$

$$-\,u_{ij}\,\overline{P}_{ij} \;\le\; P_{ij} \;\le\; u_{ij}\,\overline{P}_{ij}, \quad -u_{ij}\,\overline{Q}_{ij} \;\le\; Q_{ij} \;\le\; u_{ij}\,\overline{Q}_{ij}, \quad \forall (i,j)\in\mathcal{L} \tag{39}$$

$$u_{ij} \le o_{ij} + z_{ij} - (o_{ij}\cdot z_{ij}), \quad \forall (i,j)\in\mathcal{L} \tag{40}$$

$$\delta_i \le h_i, \quad \forall i\in\mathcal{N} \tag{41}$$

$$\sum_{\{j|j\in\mathcal{L}_{R,i}^{\text{up}}\}} P_{ij} - \sum_{\{j|j\in\mathcal{L}_{R,i}^{\text{dn}}\}} P_{ij} + \sum_{\{j|j<i,\,(i,j)\in\mathcal{L}_T\}} P_{ij} - \sum_{\{j|i<j,\,(i,j)\in\mathcal{L}_T\}} P_{ij} = \delta_i\cdot P_i^{Load} \;-\; P_i^G, \quad \forall i\in\mathcal{N} \tag{42}$$

$$\sum_{\{j|j\in\mathcal{L}_{R,i}^{\text{up}}\}} Q_{ij} - \sum_{\{j|j\in\mathcal{L}_{R,i}^{\text{dn}}\}} Q_{ij} + \sum_{\{j|j<i,\,(i,j)\in\mathcal{L}_T\}} Q_{ij} - \sum_{\{j|i<j,\,(i,j)\in\mathcal{L}_T\}} Q_{ij} = \delta_i\cdot Q_i^{Load} \;-\; Q_i^G, \quad \forall i\in\mathcal{N} \tag{43}$$

$$\frac{\sum_{\{j|j\in\mathcal{L}_{R,i}^{\text{dn}}\}} h_j\,u_{ij} + \sum_{\{j|j\in\mathcal{L}_{R,i}^{\text{up}}\}} h_j\,u_{ij}}{|\mathcal{L}_i|} \;\le\; h_i \;\le\; \sum_{\{j|j\in\mathcal{L}_{R,i}^{\text{dn}}\}} h_j\,u_{ij} + \sum_{\{j|j\in\mathcal{L}_{R,i}^{\text{up}}\}} h_j\,u_{ji}, \quad \forall i\in\mathcal{N}\setminus\mathcal{S} \tag{44}$$

$$-\,M\,(1-u_{ij}) + \frac{R_{ij}P_{ij} + X_{ij}Q_{ij}}{V_0} \;\le\; V_i - V_j \;\le\; M\,(1-u_{ij}) + \frac{R_{ij}P_{ij} + X_{ij}Q_{ij}}{V_0}, \quad \forall (i,j)\in\mathcal{L} \tag{45}$$

$$\underline{V}_i \le V_i \le \overline{V}_i, \quad \forall i\in\mathcal{N} \tag{46}$$

$$\xi_{ij}^{+} + \xi_{ij}^{-} = u_{ij}, \quad \forall (i,j)\in\mathcal{L} \tag{47}$$

$$\sum_{\{j|j\in\mathcal{L}_{R,i}^{\text{up}}\}} \xi_{ij}^{+} + \sum_{\{j|j\in\mathcal{L}_{R,i}^{\text{dn}}\}} \xi_{ij}^{-} \;\le\; \lambda_{\max}, \quad \forall i\in\mathcal{N}\setminus\mathcal{S} \tag{48}$$

$$\sum_{i\in\mathcal{S}} \left[\sum_{\{j|j\in\mathcal{L}_{R,i}^{\text{up}}\}} \xi_{ij}^{+} + \sum_{\{j|j\in\mathcal{L}_{R,i}^{\text{dn}}\}} \xi_{ij}^{-} \right] \;\le\; \lambda_{\max} \tag{49}$$

$$\tag{50}$$

The constraint framework ensures feasible resilience investment strategies through several key mechanisms: DG penetration and deployment limits (constraints 35-36) maintain reasonable distributed generation integration levels; hardening budget constraint (37) reflects realistic capital investment limitations; DG output limits (38) couple generation capacity with installation decisions; line flow constraints (39) prevent thermal overloading; hardening logic constraint (40) links line availability with fault conditions and hardening investments through the relationship $u_{ij} \le o_{ij}+z_{ij}-(o_{ij}\cdot z_{ij})$, ensuring lines are energizable only if intact or hardened; power balance equations (42-43) maintain electrical feasibility; connectivity constraints (41-44) ensure topological consistency; voltage constraints (45-46) maintain power quality; radiality constraints (47-49) preserve tree network structure with $\lambda_{\max} = (|\mathcal{N}| - |\mathcal{S}|)/(|\mathcal{N}| - |\mathcal{S}| + 1)$.

The optimization framework enables systematic comparison of resilience investment strategies across

different wind field modeling approaches, quantifying how improved meteorological characterization influences optimal infrastructure hardening decisions and demonstrating the value of high-resolution climate modeling for evidence-based resilience planning. This integrated approach ensures that capital investments in underground conversion and distributed generation deployment are optimally allocated to maximize hurricane resilience while maintaining operational feasibility under diverse failure scenarios.

Supplementary Note 12: Electricity outage cost (EOC) estimates

Converting power system load losses into quantifiable economic impacts requires a standardized methodology that accurately captures the societal costs of hurricane-induced electricity disruptions. We employ the comprehensive Electricity Outage Cost (EOC) framework developed by Woo et al.[53], which synthesizes extensive market data across all 48 contiguous United States collected by federal agencies during 2019–2020. This methodology provides robust, empirically-validated estimates of the median EOC by census region and year, representing the economic value of unserved electricity per kilowatt-hour during system interruptions.

For Virginia, our primary study region, the established average EOC equals $1.93 per kWh unserved, derived from comprehensive regional economic surveys and utility performance data. To enhance the accuracy of our economic impact assessments, we incorporate differentiated weighting factors that reflect the varying criticality of infrastructure components during emergency conditions. These weights, detailed in Supplementary Table 1, ensure that power outages affecting essential services—including hospitals, emergency response facilities, and critical communication networks—receive appropriate prioritization in the economic valuation framework, providing a more realistic representation of the societal costs associated with hurricane-induced power system failures.

The total economic impact for each hurricane scenario is calculated using the following weighted formulation:

$$\text{Economic Loss} = \sum_{i \in \mathcal{N}} (1 - \delta_i) \omega_i P_i^{\text{shed}} \times \text{EOC} \times \text{T}_i^{out} \tag{51}$$

where $\mathcal{N}$ represents the complete set of nodes in the power distribution network, δ_i is the binary power availability indicator for node i (equal to 0 during outages and 1 when power is maintained), ω_i denotes the critical infrastructure load weighting factor for node i as specified in Supplementary Table 1 (reflecting the relative societal importance of maintaining power supply to different facility types), P_i^{shed} represents the unserved electrical load demand (in kWh) at node i during the outage period, EOC corresponds to the Virginia-specific Electricity Outage Cost valued at $1.93 per kWh unserved, and T_i^{out} denotes the duration of power interruption (in hours) at node i.

For comparative analyses evaluating different wind field modeling approaches under identical hurricane scenarios, we maintain consistent outage duration assumptions across all simulations to isolate the economic impact attributable solely to variations in meteorological representation fidelity. This methodological approach enables direct quantification of how enhanced wind field modeling translates into measurable economic benefits through improved resilience planning effectiveness.

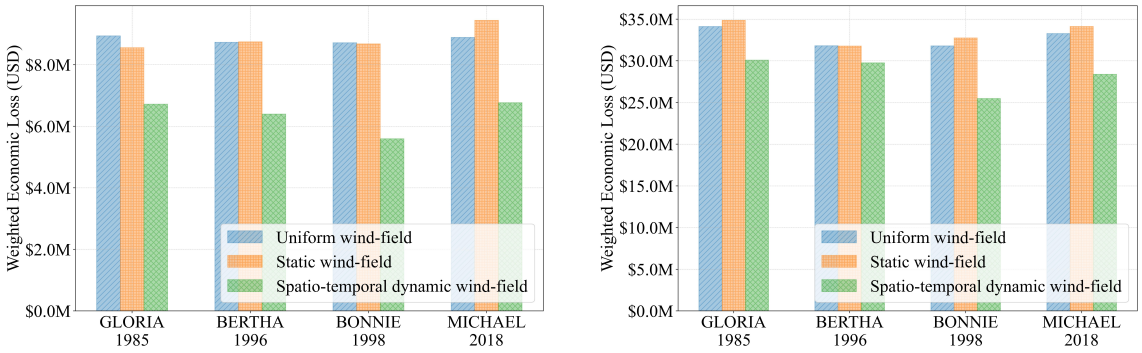

Supplementary Figure 15: Weighted economic losses after resilience optimization under different wind-field modeling approaches for (a), Suffolk City and (b), Chesapeake City. Bar charts demonstrate that high-spatio-temporal-resolution (HSTR) dynamic wind field modeling consistently reduces economic losses compared to uniform and static peak wind models across all hurricane approach directions, providing quantitative validation of the economic benefits achievable through enhanced meteorological data integration in urban power distribution networks planning.

Supplementary Note 13: Geographic heterogeneity in long-term hurricane risk assessment using synthetic event generation

Comprehensive urban resilience planning requires systematic understanding of how hurricane exposure varies across geographic gradients, as coastal proximity, topographic characteristics, and physiographic setting create spatially heterogeneous vulnerability profiles that fundamentally influence optimal infrastructure investment strategies. We examine three representative Virginia municipalities spanning distinct coastal-to-inland exposure gradients to quantify how geographic position influences long-term hurricane climatology and determines differentiated resilience investment requirements.

Our comparative framework encompasses Williamsburg (coastal tidewater region experiencing maximum Atlantic hurricane exposure), Fairfax (transitional Piedmont zone encountering attenuated but significant storm impacts), and Galax (interior Appalachian location with minimal direct hurricane influence). This geographic transect captures the complete spectrum of hurricane risk conditions across Virginia's diverse physiographic provinces, enabling systematic assessment of how storm climatology variations should inform location-specific resilience planning strategies. The geographic and environmental characteristics of these study regions reveal fundamental differences in elevation, land cover, and development patterns that influence both hurricane exposure and infrastructure vulnerability conditions.

(a)

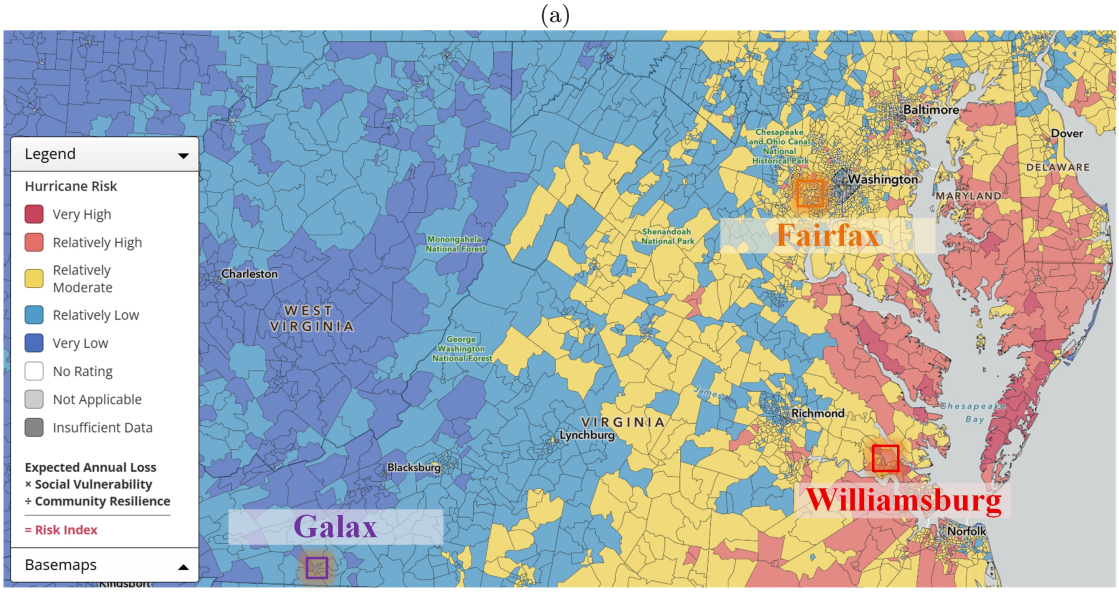

(b)

Supplementary Figure 16: Distribution of the National Hurricane Risk Index as determined by FEMA (a) Regional context showing locations relative to Atlantic hurricane tracks and physiographic boundaries. (b) Distribution of the National Hurricane Risk Index

Supplementary Figure 16 shows the distribution of the National Hurricane Risk Index as determined by FEMA [54], confirming the high-risk, moderate-risk, and low-risk characteristics of Williamsburg, Fairfax, and Galax, respectively.

We construct high-fidelity synthetic distribution networks for each municipality using our integrated geospatial methodology detailed in Supplementary Notes 1-4, incorporating realistic infrastructure topologies, critical load distributions, and environmental characteristics that accurately reflect local development patterns and vulnerability conditions. The resulting network architectures demonstrate varying complexity and critical infrastructure distributions that correspond to each region's unique demographic and economic characteristics.

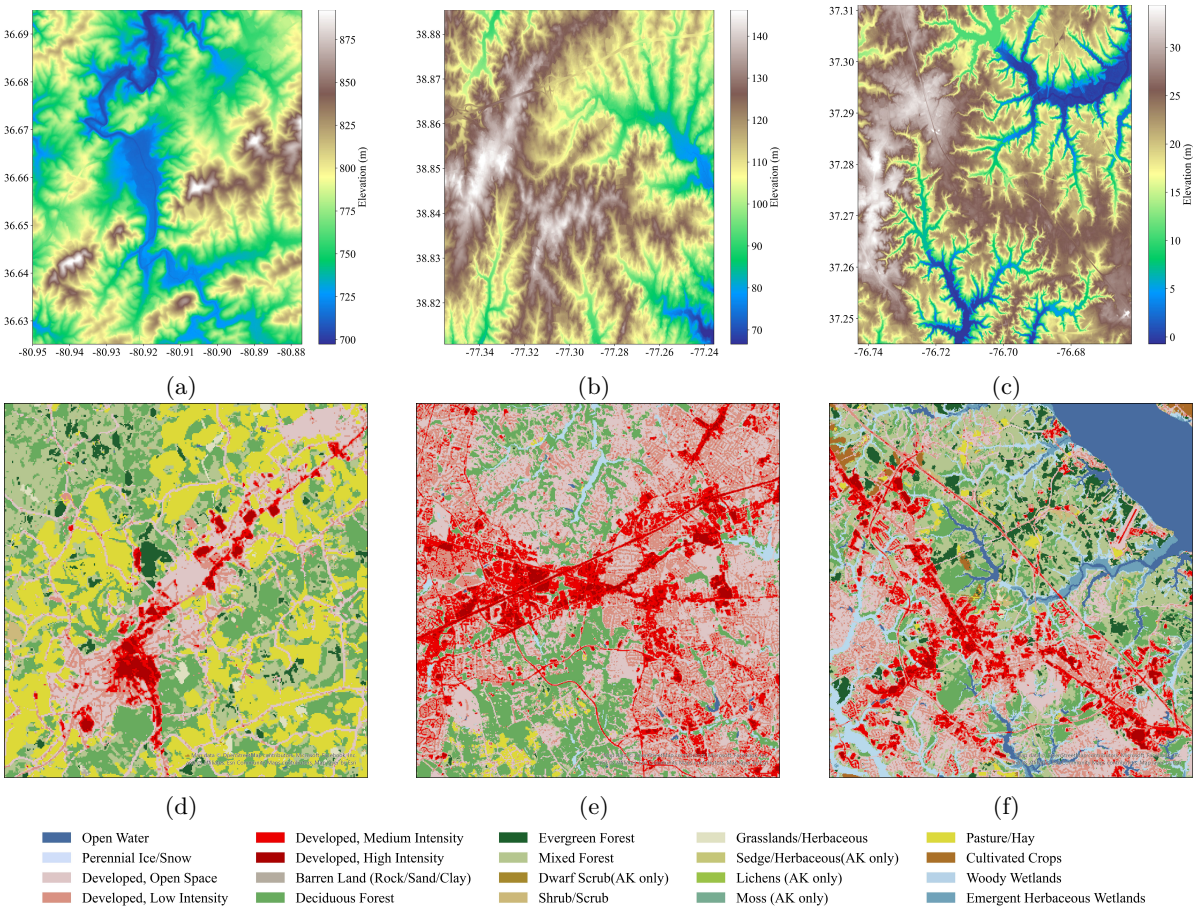

Supplementary Figure 17: Geographic and environmental characterization of representative study regions across Virginia's hurricane exposure gradient. Elevation distributions reveal topographic diversity: (a) Galax, (b) Fairfax, (c) Williamsburg. Land cover classifications demonstrate varying environmental conditions: (d) Galax, (e) Fairfax, (f) Williamsburg, illustrating how geographic setting influences both hurricane exposure and infrastructure vulnerability patterns.

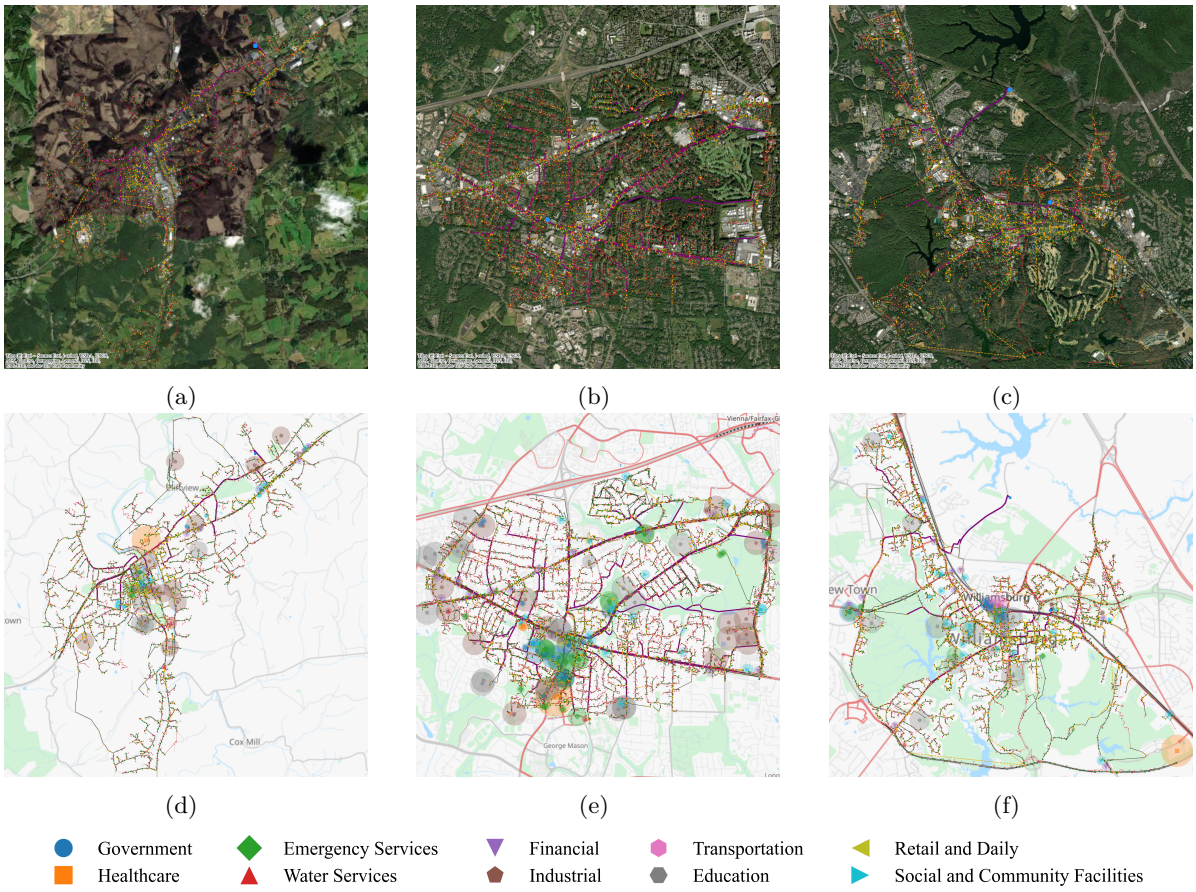

Supplementary Figure 18: Synthetic distribution network architectures reflecting regional infrastructure characteristics. Network topologies demonstrate varying complexity: (a) Galax, (b) Fairfax, (c) Williamsburg. Critical infrastructure classifications reveal different vulnerability profiles: (d) Galax, (e) Fairfax, (f) Williamsburg, illustrating how local development patterns influence both network structure and resilience requirements for hurricane preparedness.

To establish comprehensive hurricane climatology, we analyze the complete IBTrACS archive spanning 1840-2024, encompassing 184 years of Atlantic basin tropical cyclone activity. This extended temporal perspective captures the full range of hurricane variability including multi-decadal oscillations and low-frequency climate patterns that influence regional storm activity. Each historical event undergoes climate adjustment using Knutson parameterization to ensure consistency with projected mid-century conditions.

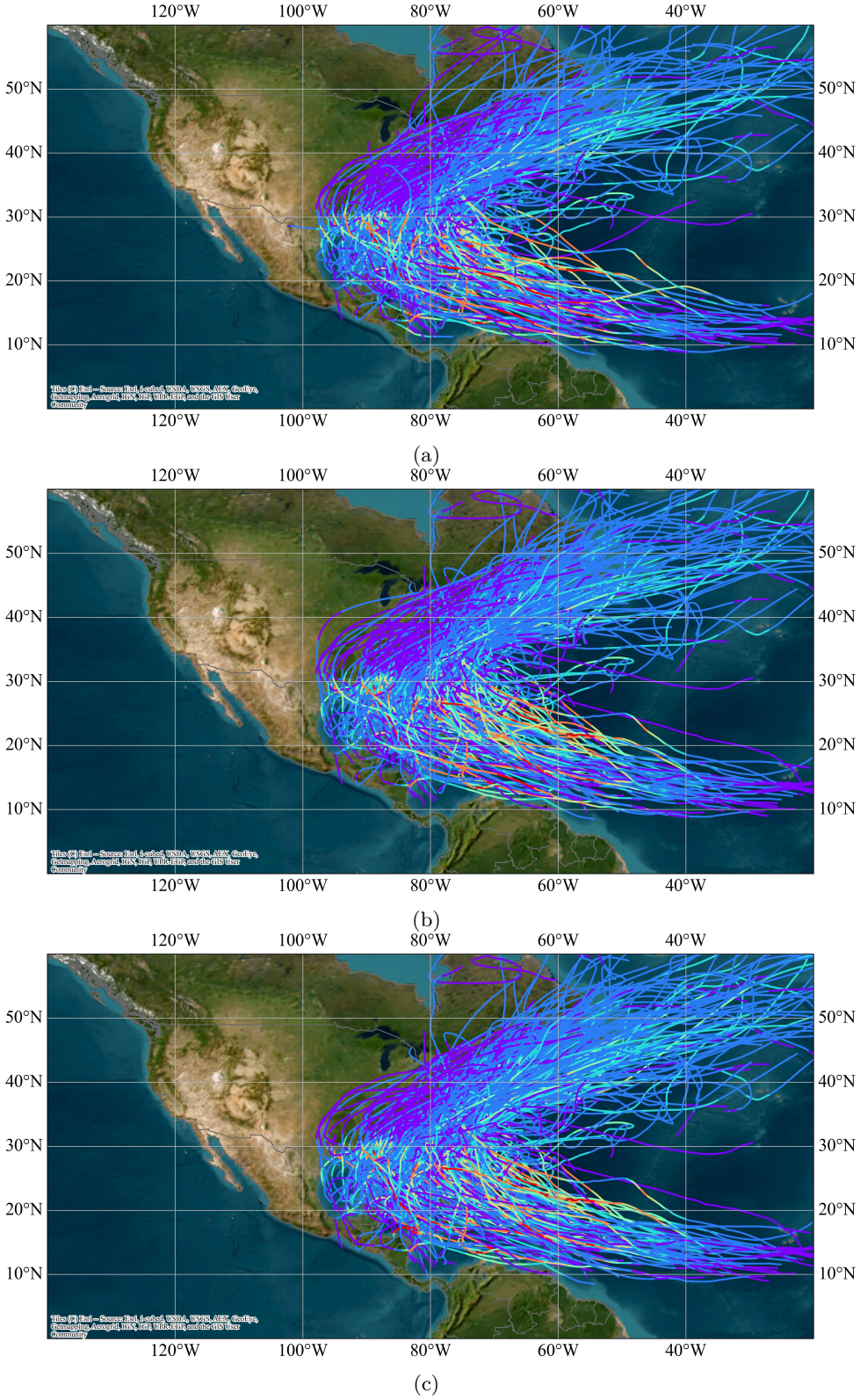

Supplementary Figure 19: Comprehensive hurricane climatology across Virginia's geographic gradient (1840-2024) revealing systematic variation in storm frequency and intensity. Historical track analysis demonstrates decreasing hurricane exposure with distance from coast: (a) Galax experiences minimal direct impacts, (b) Fairfax encounters moderate exposure, (c) Williamsburg faces maximum coastal vulnerability. Track density patterns reflect the fundamental role of geographic position in determining long-term hurricane risk profiles essential for differentiated resilience planning strategies.

Historical hurricane records, while extensive, provide limited statistical power for characterizing ex-

treme event probabilities that are essential for infrastructure design and resilience planning. To address this limitation, we apply a synthetic hurricane generation methodology based on the CLIMADA framework that systematically expands the available event catalog while preserving realistic storm trajectory and intensity characteristics.

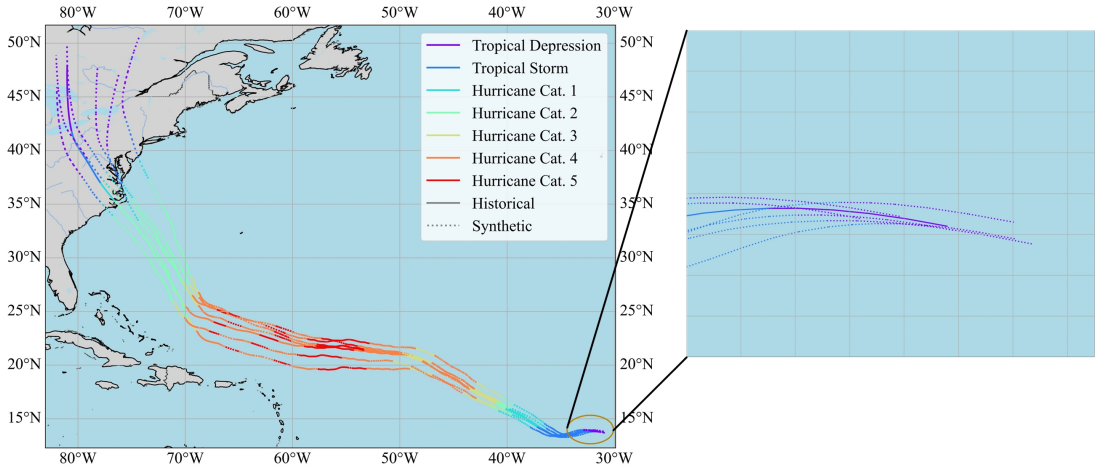

Supplementary Figure 20: Synthetic hurricane trajectory generation methodology for extreme event simulation. The perturbation framework introduces realistic variability through (1) initial position uncertainty reflecting natural storm genesis variations, (2) directional angle perturbations modeling atmospheric steering uncertainties, and (3) translational velocity fluctuations capturing speed variations, enabling generation of physically plausible hurricane ensembles that significantly expand the statistical foundation for extreme event analysis and infrastructure vulnerability assessment.

Synthetic hurricane generation employs a physics-based perturbation methodology that introduces controlled variability in three key trajectory characteristics. Initial position perturbation models spatial uncertainty in storm genesis locations through uniform random offsets:

$$\lambda_0^{(k)} = \lambda_0 + \xi_\lambda, \quad \phi_0^{(k)} = \phi_0 + \xi_\phi, \tag{52}$$

where $\xi_\lambda, \xi_\phi \sim U(-0.75\check{r}, 0.75\check{r})$ represent longitude and latitude offsets calibrated from IBTrACS storm spacing analysis to ensure realistic geographic dispersion.

Directional angle perturbation captures cumulative steering flow uncertainties through temporally correlated angular deflections:

$$\theta_i^{\text{pert}} = \theta_i + \sum_{j=1}^{i} \eta_j, \quad \eta_j \sim \mathcal{N}(0, \sigma_\theta^2), \tag{53}$$

where the disturbance follows first-order autoregression $\eta_j = \alpha_\theta \eta_{j-1} + \epsilon_j$ with $\alpha_\theta = 0.5$ ensuring trajectory continuity and $\sigma_\theta = \pi/360$ rad/h limiting deflection magnitude to realistic values.

Translational velocity perturbation models storm speed variations through correlated relative adjustments:

$$v_i^{(k)} = v_i \cdot (1 + \delta v_i), \quad \delta v_i \sim \mathcal{N}(0, \sigma_v^2), \tag{54}$$

where $\delta v_i = \alpha_v \delta v_{i-1} + \zeta_i$ with $\alpha_v = 0.85$ reflecting hurricane movement inertia and $\sigma_v = 0.3$ calibrated from historical speed variability analysis.

Trajectory evolution employs spherical great-circle geometry with landfall-dependent exponential decay ($\kappa_v = 0.15$ h^{-1}) implemented through the CLIMADA framework, ensuring physically consistent hurricane behavior across oceanic and terrestrial environments.

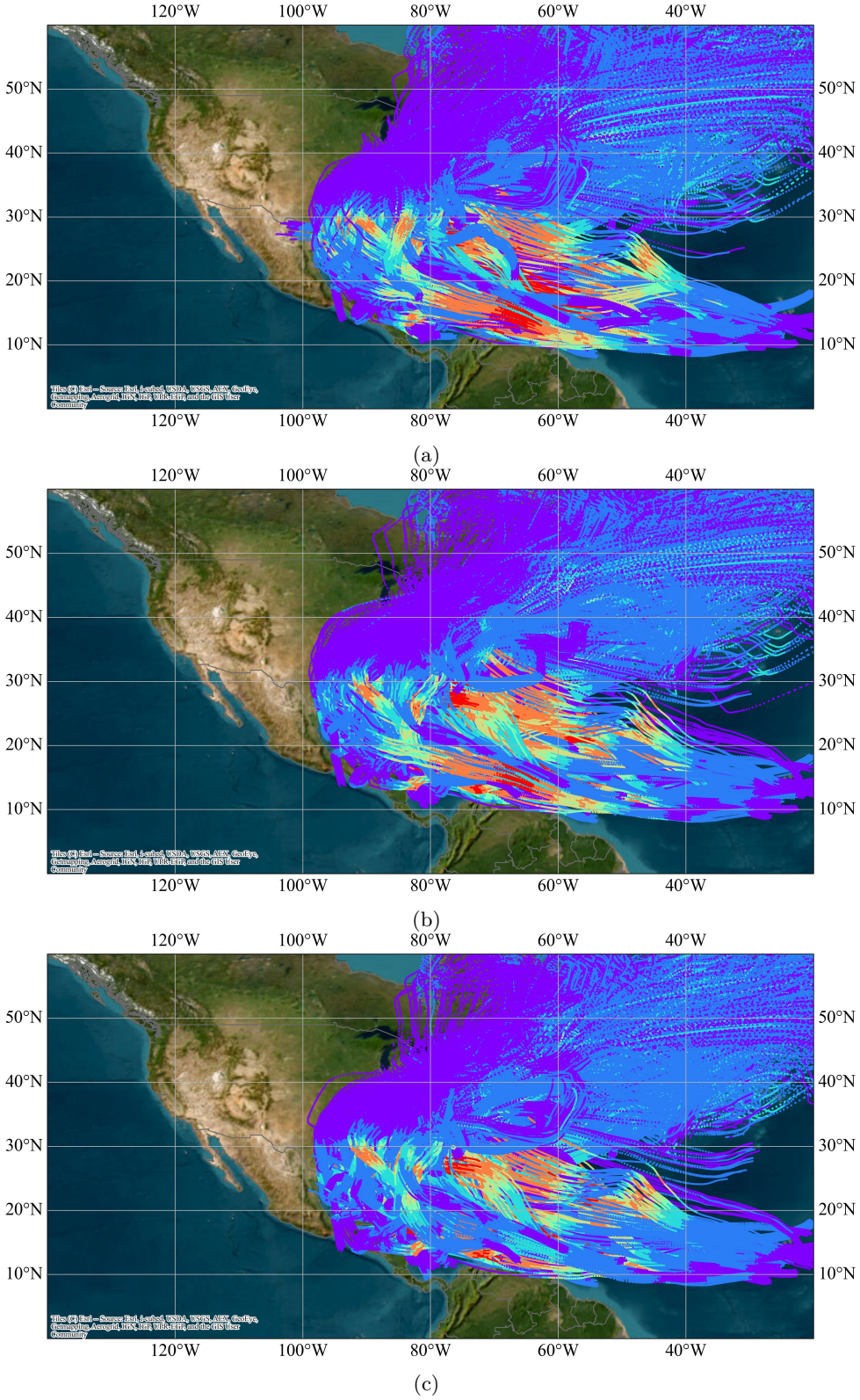

Supplementary Figure 21: Synthetic hurricane ensemble expansion for robust statistical analysis. Twenty-fold perturbation of historical storm catalog generates comprehensive event sets enabling robust extreme value analysis: (a) Galax (8,062 synthetic events), (b) Fairfax (8,119 synthetic events), (c) Williamsburg (9,793 synthetic events). Enhanced statistical power facilitates reliable characterization of rare, high-consequence events critical for infrastructure design standards and enables quantification of tail risk behavior essential for climate-informed resilience planning across diverse geographic contexts.

The synthetic generation process produces over 8,000 hurricane realizations for each municipality,

providing robust statistical foundations for extreme value analysis. We characterize regional wind speed distributions using three-parameter Weibull models, enabling quantitative comparison of tail behavior that determines infrastructure design requirements and resilience investment priorities across the coastal-inland exposure gradient.

Supplementary Note 14: Stochastic optimization framework for climate-resilient urban power distribution networks

We develop a comprehensive stochastic optimization framework that integrates climate-specific hurricane risks into resilience planning for urban power distribution networks. The framework employs Conditional Value at Risk (CVaR) within a two-stage stochastic programming approach, enabling decision-makers to systematically balance expected system performance against extreme weather event risks. The risk preference parameter λ controls the trade-off between expected performance and tail-risk protection, allowing for flexible adaptation to different risk tolerance levels.

Our model incorporates representative failure scenarios Γ_h for each hurricane event $h \in H$, with scenario probabilities p_h derived from maximum sustained wind speeds and city-specific wind vulnerability profiles. The decision framework encompasses two key investment strategies: distributed generation (DG) deployment and transmission line hardening. Decision variables $\mathbf{R}$ include DG placement indicators (c_i), generation capacities (β_i), maximum allowable units ($C_{\max}$), system penetration limits ($\theta_{\max}$), line hardening selections (z_{ij}), and hardening budget constraints ($Z_{\max}$).

The optimization objective balances expected system performance against worst-case scenario risks:

$$\min(1-\lambda)E[Q(R,\Gamma_h)] + \lambda\,\mathrm{CVaR}_\alpha(Q(R,\Gamma_h)), \tag{55}$$

where $\lambda \in [0,1]$ represents the decision-maker's risk attitude, with $\lambda = 0$ corresponding to risk-neutral planning and $\lambda = 1$ to extreme risk-averse planning. The expected weighted load loss $E[Q(R,\Gamma_h)]$ across all hurricane scenarios is defined as:

$$E[Q(R,\Gamma_h)] = \sum_{h\in H} p_h \cdot Q(R,\Gamma_h), \tag{56}$$

where the scenario-specific weighted load loss $Q(R,\Gamma_h)$ quantifies service disruption under hurricane h:

$$Q(R,\Gamma_h) = \sum_{i\in N}(1-\delta_i^h)\cdot\omega_i\cdot P_i^{Load}. \tag{57}$$

The CVaR term captures tail risk at the α quantile:

$$\mathrm{CVaR}_\alpha(Q(R,\Gamma_h)) = \eta + \frac{1}{1-\alpha}\sum_{h\in H} p_h\gamma_h, \tag{58}$$

where δ_i^h is the binary load-shedding variable for node i under hurricane scenario h (0 indicates load disconnection), ω_i represents the criticality-weighted load factor at node i, P_i^{Load} denotes the load demand, η represents the Value-at-Risk (VaR) at confidence level α, and γ_h is an auxiliary variable that linearizes the CVaR formulation by capturing excess load loss beyond η for each scenario.

To evaluate the impact of high-resolution historical climate data on risk-informed resilience planning, we implemented this framework across three representative Virginia cities: Galax, Fairfax, and Williamsburg. Each city's analysis incorporated 50 years of historical storm records. Following climate adjustment procedures, we extracted maximum sustained wind speeds at the point of closest approach for each historical event and derived corresponding scenario probabilities from fitted Weibull wind-speed distributions specific to each location. These empirically-derived wind-speed–probability pairs serve as stochastic hazard inputs to our optimization model.

The optimization framework is structured as a two-stage program. First-stage decisions determine long-term infrastructure investments in DG deployment and line hardening, subject to resource con-

straints:

$$\sum_{i\in N} c_i\beta_i \le \theta_{\max}, \tag{59}$$

$$\sum_{i\in N} c_i \le C_{\max}, \tag{60}$$

$$\sum_{(i,j)\in L} z_{ij} \le Z_{\max}. \tag{61}$$

$$\tag{62}$$

Second-stage operational constraints govern emergency response through network reconfiguration and islanding strategies:

$$0 \;\le\; P_i^G \;\le\; \overline{P}_i^G, \quad 0 \;\le\; Q_i^G \;\le\; \overline{Q}_i^G, \quad \forall i \in \big(S \cup G\big), \tag{63}$$

$$-\,u_{ij}\,\overline{P}_{ij} \;\le\; P_{ij} \;\le\; u_{ij}\,\overline{P}_{ij}, \quad -u_{ij}\,\overline{Q}_{ij} \;\le\; Q_{ij} \;\le\; u_{ij}\,\overline{Q}_{ij}, \quad \forall (i,j) \in L, \tag{64}$$

$$u_{ij} \le o_{ij} + z_{ij} - (o_{ij} \cdot z_{ij}), \quad \forall (i,j) \in L, \tag{65}$$

$$\delta_i \le h_i, \quad \forall i \in N, \tag{66}$$

$$\sum_{\{\,j|j\in L^{\mathrm{up}}_{R,i}\}} P_{ij} - \sum_{\{\,j|j\in L^{\mathrm{dn}}_{R,i}\}} P_{ij} + \sum_{\{\,j|j<i,\,(i,j)\in L_T\}} P_{ij} - \sum_{\{\,j|i<j,\,(i,j)\in L_T\}} P_{ij} = \delta_{i,t}\cdot P_i^{Load} \;-\; P_i^G, \quad \forall i \in N, \tag{67}$$

$$\sum_{\{\,j|j\in L^{\mathrm{up}}_{R,i}\}} Q_{ij} - \sum_{\{\,j|j\in L^{\mathrm{dn}}_{R,i}\}} Q_{ij} + \sum_{\{\,j|j<i,\,(i,j)\in L_T\}} Q_{ij} - \sum_{\{\,j|i<j,\,(i,j)\in L_T\}} Q_{ij} = \delta_{i,t}\cdot Q_i^{Load} \;-\; Q_i^G, \quad \forall i \in N, \tag{68}$$

$$\frac{\sum_{\{\,j|j\in L^{\mathrm{dn}}_{R,i}\}} h_j\,u_{ij} + \sum_{\{\,j|j\in L^{\mathrm{up}}_{R,i}\}} h_j\,u_{ij}}{|L_i|} \;\le\; h_i \;\le\; \sum_{\{\,j|j\in L^{\mathrm{dn}}_{R,i}\}} h_j\,u_{ij} + \sum_{\{\,j|j\in L^{\mathrm{up}}_{R,i}\}} h_j\,u_{ji}, \quad \forall i \in N\setminus S, \tag{69}$$

$$-\,M\left(1-u_{ij}\right) + \frac{R_{ij}P_{ij} + X_{ij}Q_{ij}}{V_0} \;\le\; V_i - V_j \;\le\; M\left(1-u_{ij}\right) + \frac{R_{ij}P_{ij} + X_{ij}Q_{ij}}{V_0}, \quad \forall (i,j) \in L, \tag{70}$$

$$\underline{V}_i \le V_i \le \overline{V}_i, \quad \forall i \in N, \tag{71}$$

$$\xi_{ij}^{+} + \xi_{ij}^{-} = u_{ij}, \quad \forall (i,j) \in L, \tag{72}$$

$$\sum_{\{\,j|j\in L^{\mathrm{up}}_{R,i}\}} \xi_{ij}^{+} + \sum_{\{\,j|j\in L^{\mathrm{dn}}_{R,i}\}} \xi_{ij}^{-} \;\le\; \lambda_{\max}, \quad \forall i \in N\setminus S, \tag{73}$$

$$\sum_{i\in S}\Big[\sum_{\{\,j|j\in L^{\mathrm{up}}_{R,i}\}} \xi_{ij}^{+} + \sum_{\{\,j|j\in L^{\mathrm{dn}}_{R,i}\}} \xi_{ij}^{-}\Big] \;\le\; \lambda_{\max}, \tag{74}$$

$$\gamma_h \ge Q(R,\Gamma_h) - \eta, \quad \gamma_h \in \mathbb{R}_+^n. \tag{75}$$

The mathematical formulation employs standard power system notation. Set N represents all network buses with subset $S \subseteq N$ denoting substation nodes and $G \subseteq N$ denoting nodes with DG installations. Set L encompasses all transmission lines, partitioned into regular lines L_R and normally-open tie-lines L_T. For each node i, L_i denotes the set of incident lines. Binary variable h_i indicates node energization status, while u_{ij} represents the switching state of line (i,j). Parameter $o_{ij} = 0$ indicates storm-induced line outages (intact lines have $o_{ij} = 1$). Variables P_{ij}, Q_{ij} represent active and reactive power flows, while P_i^G, Q_i^G denote DG outputs bounded by capacities $\overline{P}_i^G$, $\overline{Q}_i^G$. Line thermal limits are $\overline{P}_{ij}$, $\overline{Q}_{ij}$. Voltage variables include squared magnitude V_i, line impedance parameters R_{ij}, X_{ij}, and base voltage V_0. The radiality constraint employs maximum connection ratio $\lambda_{\max} = (|N| - |S|)/(|N| - |S| + 1)$ with auxiliary variables $\xi_{ij}^{\pm}$ ensuring tree topology.

Constraints (67)–(68) enforce active and reactive power balance. Constraints (63)–(64) impose generator output and line flow limits. Constraint (65) links line switching status with outage states and hardening decisions. Constraint (66) prevents load supply from de-energized nodes. Constraint (69) applies the Distflow power flow constraints. Constraints (70)–(71) represent linearized voltage drop equations and bounds. Radiality preservation is enforced through constraints (72)–(74) using density-based formulations that prevent loop formation [52]. Constraint (75) defines auxiliary variables for CVaR computation.

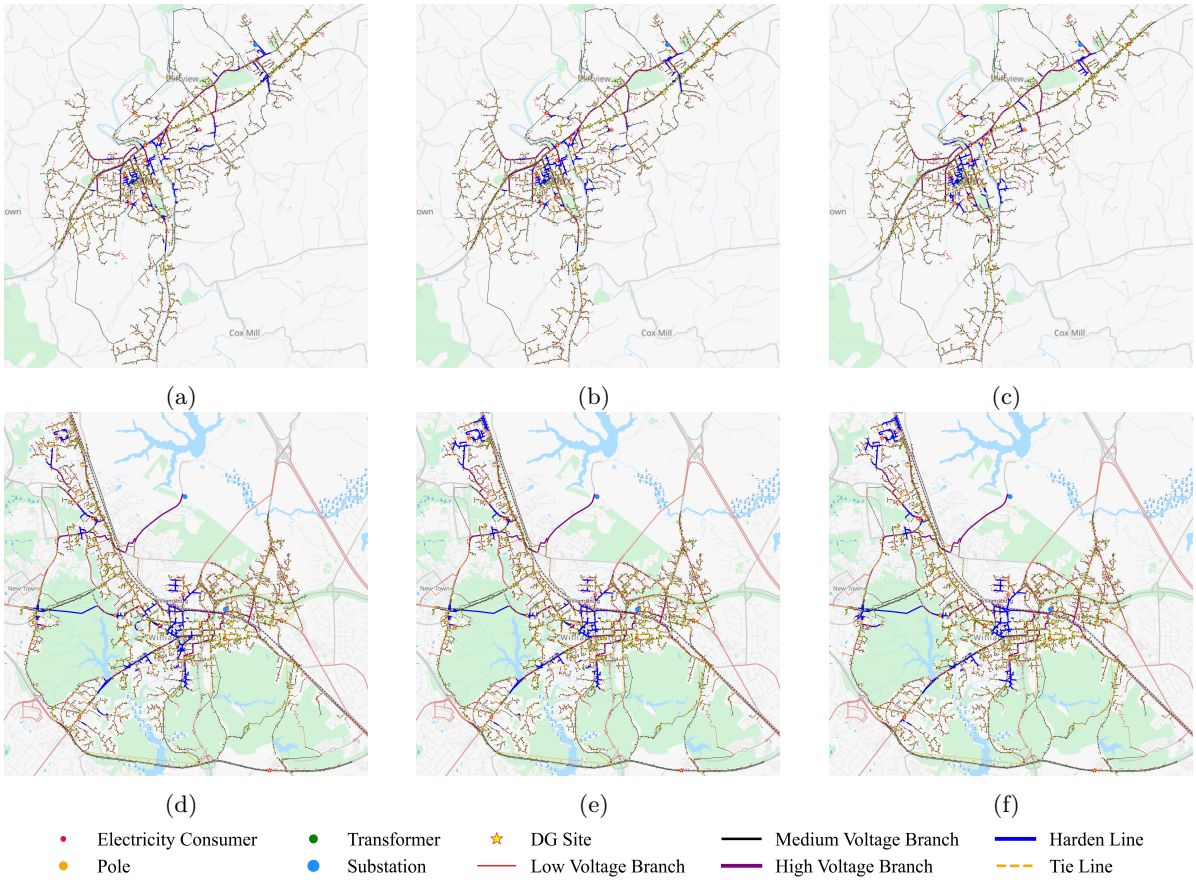

Supplementary Figure 22: Risk attitude significantly influences optimal infrastructure investment patterns. Results compare distributed generation deployment and line hardening strategies under varying risk preferences for (a)–(c)) Galax and (d)–(f) Williamsburg. Risk-seeking planners ($\lambda \approx 0$) prioritize cost-effective expected performance, while risk-averse planners ($\lambda \approx 1$) emphasize protection against worst-case scenarios. Risk-neutral strategies ($\lambda = 0.5$) balance both objectives. Each case assumes deployment of 10 DG units with hardening of 10% of transmission lines.

(a) 5% hardening budget (b) 10% hardening budget (c) 15% hardening budget

(d) 20% hardening budget (e) 25% hardening budget (f) 30% hardening budget

(g) 35% hardening budget (h) 40% hardening budget (i) 45% hardening budget

(j) 50% hardening budget (k) 55% hardening budget (l) 60% hardening budget

Supplementary Figure 23: Optimal underground cable deployment strategies under risk-seeking planning for the Galax distribution network across hardening budget allocations from 5% to 60%.

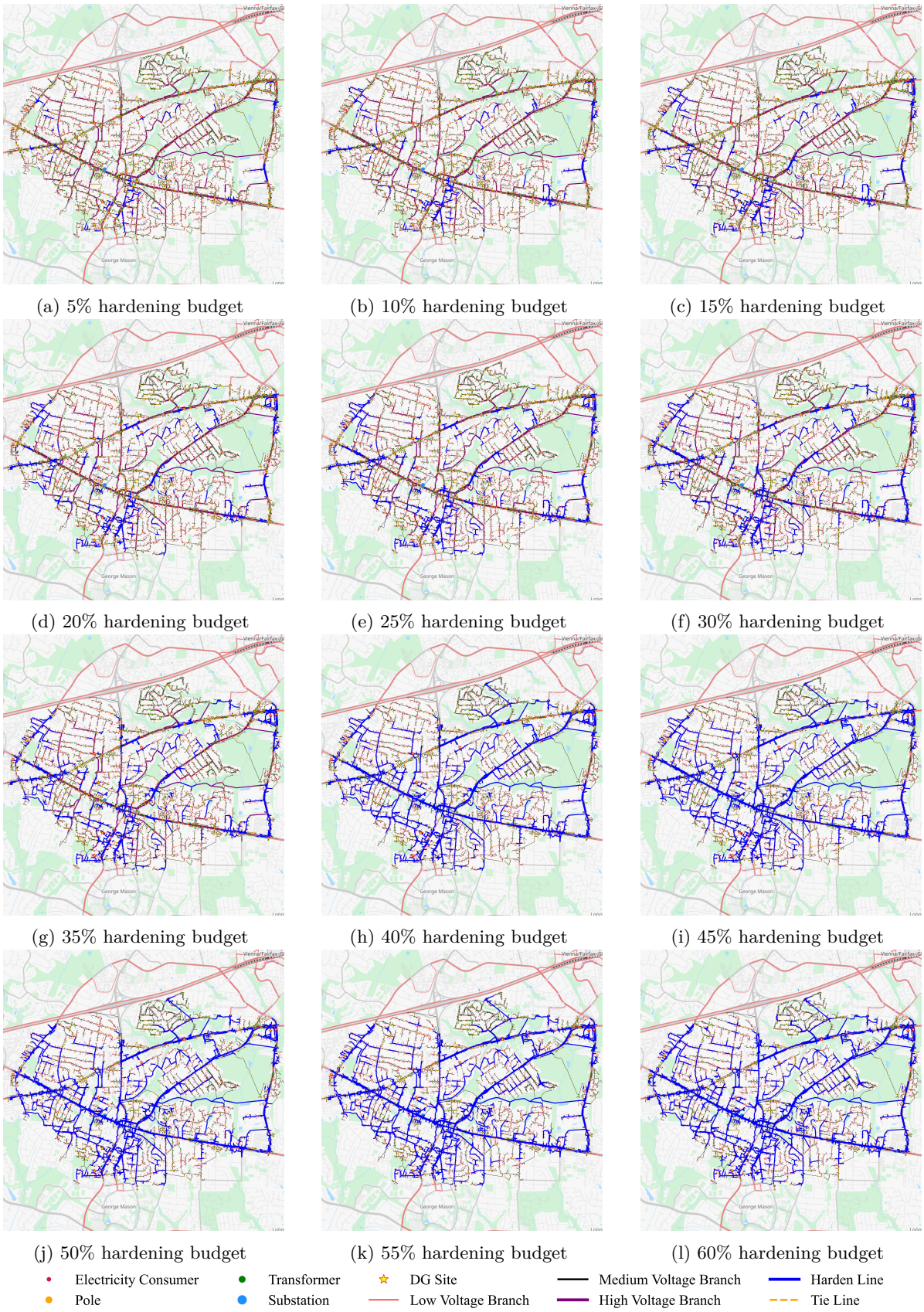

Supplementary Figure 24: Optimal underground cable deployment strategies under risk-seeking planning for the Fairfax distribution network across hardening budget allocations from 5% to 60%.

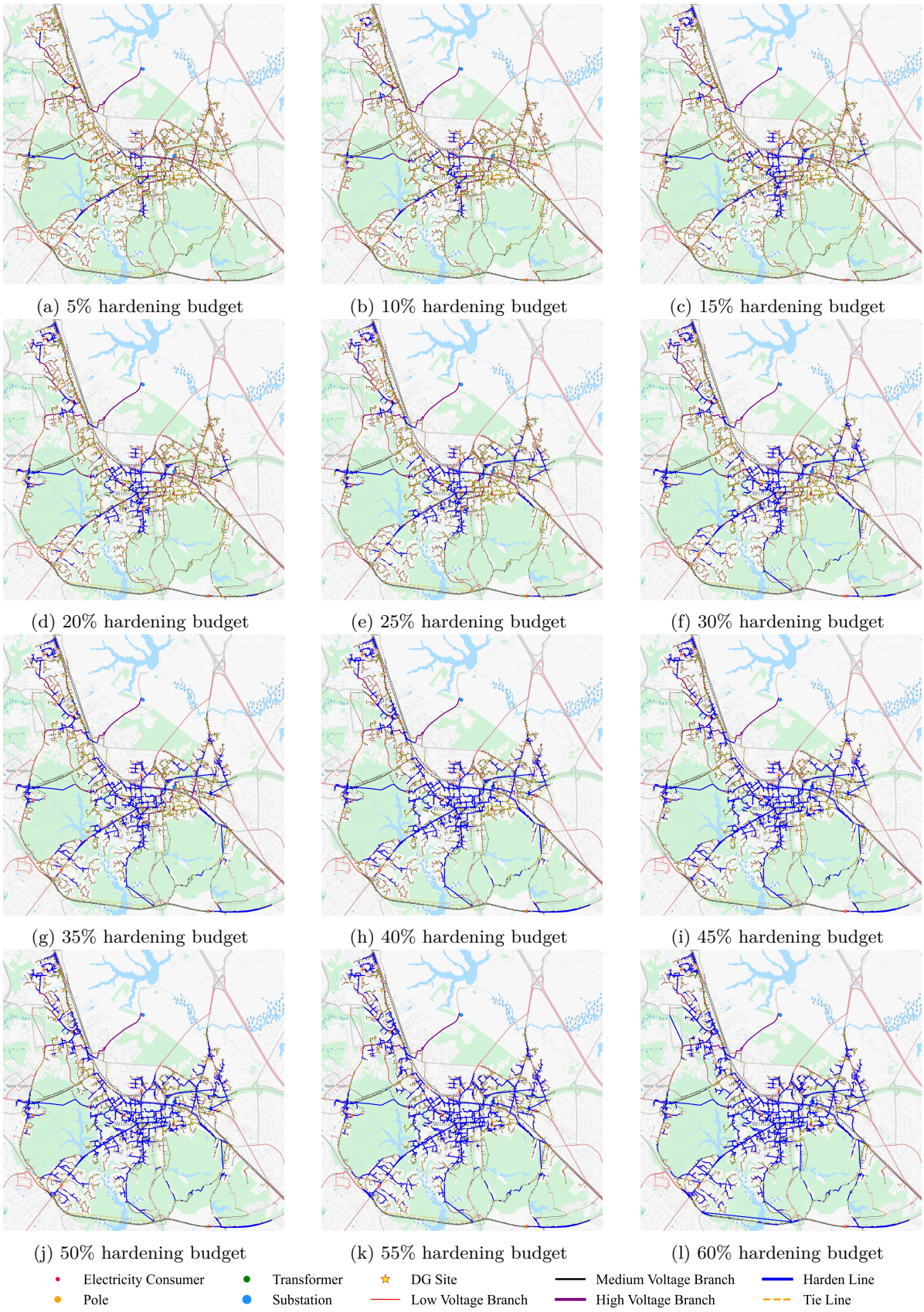

Supplementary Figure 25: Optimal underground cable deployment strategies under risk-seeking planning for the Williamsburg distribution network across hardening budget allocations from 5% to 60%.

References

[1] Meyur, R. *et al.* Creating realistic power distribution networks using interdependent road infrastructure. In *2020 IEEE International Conference on Big Data (Big Data)*, 1226–1235 (2020).

[2] Postigo Marcos, F. E. *et al.* A review of power distribution test feeders in the united states and the need for synthetic representative networks. *Energies* **10**, 1896 (2017).

[3] Meyur, R. *et al.* Ensembles of realistic power distribution networks. *Proc. Natl. Acad. Sci. U.S.A.* **119**, e2205772119 (2022).

[4] Florida Power & Light Company. How we restore power (2025). URL https://www.fpl.com/content/dam/fplgp/us/en/storm/images/en_us/HowWeRestorePower.pdf.

[5] Entergy Corporation. The restoration process is done in an orderly, deliberate manner. https://www.entergy.com/stormcenter/restoration (2024).

[6] United States Geological Survey. United states geological survey 3d elevation program 1/3 arc-second digital elevation model (2021). URL https://doi.org/10.5069/G98K778D. Distributed by OpenTopography.

[7] U.S. Geological Survey (USGS). Annual nlcd collection 1 science products (2024). URL https://doi.org/10.5066/P94UXNTS. U.S. Geological Survey data release.

[8] Gahtan, J. *et al.* International best track archive for climate stewardship (ibtracs) project, version 4r01. https://doi.org/10.25921/82ty-9e16 (2024). NOAA National Centers for Environmental Information.

[9] Purvis, J. C., Sidlow, S. F., Smith, D. J., Tyler, W. & Turner, I. Hurricane hugo. Tech. Rep., South Carolina State Climatology Office (1990). URL https://www.dnr.sc.gov/climate/sco/hurricanes/pdfs/HurricaneHugo1989.pdf.

[10] Beven, J. & Cobb, H. Tropical cyclone report: Hurricane isabel. Tech. Rep., National Hurricane Center (2014). URL https://www.nhc.noaa.gov/data/tcr/AL132003_Isabel.pdf.

[11] Stewart, S. R. & Berg, R. Tropical cyclone report: Hurricane florence. Tech. Rep., National Hurricane Center (2019). URL https://www.nhc.noaa.gov/data/tcr/AL062018_Florence.pdf.

[12] Hagen, A. B., Cangialosi, J. P., Chenard, M., Alaka, L. & Delgado, S. Tropical cyclone report: Hurricane helene. Tech. Rep., National Hurricane Center (2025). URL https://www.nhc.noaa.gov/data/tcr/AL092024_Helene.pdf.

[13] Reinhart, B. J., Reinhart, A. & Alaka, L. Tropical cyclone report: Hurricane debby. Tech. Rep., National Hurricane Center (2025). URL https://www.nhc.noaa.gov/data/tcr/AL042024_Debby.pdf.

[14] Brown, D. P., Hagen, A. & Alaka, L. Tropical cyclone report: Tropical storm ophelia. Tech. Rep., National Hurricane Center (2024). URL https://www.nhc.noaa.gov/data/tcr/AL162023_Ophelia.pdf.

[15] II, J. L. B. & Alaka, L. Tropical cyclone report: Hurricane nicole. Tech. Rep., National Hurricane Center (2023). URL https://www.nhc.noaa.gov/data/tcr/AL172022_Nicole.pdf.

[16] Bucci, L., Alaka, L., Hagen, A., Delgado, S. & Beven, J. Tropical cyclone report: Hurricane ian. Tech. Rep., National Hurricane Center (2023). URL https://www.nhc.noaa.gov/data/tcr/AL092022_Ian.pdf.

[17] Berg, R. Tropical cyclone report: Tropical storm fred. Tech. Rep., National Hurricane Center (2021). URL https://www.nhc.noaa.gov/data/tcr/AL062021_Fred.pdf.

[18] Cangialosi, J. P., Delgado, S. & Berg, R. Tropical cyclone report: Hurricane elsa. Tech. Rep., National Hurricane Center (2022). URL https://www.nhc.noaa.gov/data/tcr/AL052021_Elsa.pdf.

[19] Reinhart, B. J. & Berg, R. Tropical cyclone report: Tropical storm wanda. Tech. Rep., National Hurricane Center (2022). URL https://www.nhc.noaa.gov/data/tcr/AL212021_Wanda.pdf.

[20] Latto, A., Hagen, A. & Berg, R. Tropical cyclone report: Hurricane isaias. Tech. Rep., National Hurricane Center (2021). URL https://www.nhc.noaa.gov/data/tcr/AL092020_Isaias.pdf.

[21] Blake, E., Berg, R. & Hagen, A. Tropical cyclone report: Hurricane zeta. Tech. Rep., National Hurricane Center (2021). URL https://www.nhc.noaa.gov/data/tcr/AL282020_Zeta.pdf.

[22] Avila, L. A., Stewart, S. R., Berg, R. & Hagen, A. B. Tropical cyclone report: Hurricane dorian. Tech. Rep., National Hurricane Center (2020). URL https://www.nhc.noaa.gov/data/tcr/AL052019_Dorian.pdf.

[23] II, J. L. B., Berg, R. & Hagen, A. Tropical cyclone report: Hurricane michael. Tech. Rep., National Hurricane Center (2018). URL https://www.nhc.noaa.gov/data/tcr/AL142018_Michael.pdf.

[24] Berg, R. Tropical cyclone report: Tropical storm cindy. Tech. Rep., National Hurricane Center (2018). URL https://www.nhc.noaa.gov/data/tcr/AL032017_Cindy.pdf.

[25] Berg, R. Tropical cyclone report: Hurricane hermine. Tech. Rep., National Hurricane Center (2017). URL https://www.nhc.noaa.gov/data/tcr/AL092016_Hermine.pdf.

[26] Pasch, R. J. & Penny, A. B. Tropical cyclone report: Tropical storm colin. Tech. Rep., National Hurricane Center (2017). URL https://www.nhc.noaa.gov/data/tcr/AL032016_Colin.pdf.

[27] Stewart, S. R. Tropical cyclone report: Hurricane matthew. Tech. Rep., National Hurricane Center (2017). URL https://www.nhc.noaa.gov/data/tcr/AL142016_Matthew.pdf.

[28] Blake, E. S., Kimberlain, T. B., Berg, R. J., Cangialosi, J. P. & II, J. L. B. Tropical cyclone report: Hurricane sandy. Tech. Rep., National Hurricane Center (2013). URL https://www.nhc.noaa.gov/data/tcr/AL182012_Sandy.pdf.

[29] Avila, L. A. & Cangialosi, J. Tropical cyclone report: Hurricane irene. Tech. Rep., National Hurricane Center (2011). URL https://www.nhc.noaa.gov/data/tcr/AL092011_Irene.pdf.

[30] Brown, D. P. & Kimberlain, T. Tropical cyclone report: Hurricane hanna. Tech. Rep., National Hurricane Center (2008). URL https://www.nhc.noaa.gov/data/tcr/AL082008_Hanna.pdf.

[31] Knabb, R. D. & Mainelli, M. Tropical cyclone report: Hurricane ernesto. Tech. Rep., National Hurricane Center (2006). URL https://www.nhc.noaa.gov/data/tcr/AL062006_Ernesto.pdf.

[32] Stewart, S. R. Tropical cyclone report: Hurricane cindy. Tech. Rep., National Hurricane Center (2006). URL https://www.nhc.noaa.gov/data/tcr/AL032005_Cindy.pdf.

[33] Pasch, R. J., Brown, D. P. & Blake, E. S. Tropical cyclone report: Hurricane charley. Tech. Rep., National Hurricane Center (2011). URL https://www.nhc.noaa.gov/data/tcr/AL032004_Charley.pdf.

[34] II, J. L. B. Tropical cyclone report: Hurricane frances. Tech. Rep., National Hurricane Center (2014). URL https://www.nhc.noaa.gov/data/tcr/AL062004_Frances.pdf.

[35] Stewart, S. R. Tropical cyclone report: Hurricane ivan. Tech. Rep., National Hurricane Center (2011). URL https://www.nhc.noaa.gov/data/tcr/AL092004_Ivan.pdf.

[36] Pasch, R. J., Kimberlain, T. B. & Stewart, S. R. Preliminary report: Hurricane floyd. Tech. Rep., National Hurricane Center (2014). URL https://www.nhc.noaa.gov/data/tcr/AL081999_Floyd.pdf.

[37] Beven, J. Preliminary report: Hurricane dennis. Tech. Rep., National Hurricane Center (2000). URL https://www.nhc.noaa.gov/data/tcr/AL051999_Dennis.pdf.

[38] Avila, L. A. Preliminary report: Hurricane bonnie. Tech. Rep., National Hurricane Center (1998). URL https://www.nhc.noaa.gov/data/tcr/AL021998_Bonnie.pdf.

[39] Pasch, R. J. Preliminary report: Tropical storm josephine. Tech. Rep., National Hurricane Center (1997). URL https://www.nhc.noaa.gov/data/tcr/AL101996_Josephine.pdf.

[40] Lawrence, M. B. Preliminary report: Hurricane bertha. Tech. Rep., National Hurricane Center (1996). URL https://www.nhc.noaa.gov/data/tcr/AL021996_Bertha.pdf.

[41] Mayfield, M. Preliminary report: Hurricane fran. Tech. Rep., National Hurricane Center (1996). URL https://www.nhc.noaa.gov/data/tcr/AL061996_Fran.pdf.

[42] Mayfield, M. Preliminary report: Hurricane opal. Tech. Rep., National Hurricane Center (2014). URL https://www.nhc.noaa.gov/data/tcr/AL171995_Opal.pdf.

[43] Avila, L. A. & Rappaport, E. N. Annual summaries: Atlantic hurricane season of 1994. Tech. Rep., National Hurricane Center (1996). URL https://www.nhc.noaa.gov/data/mwreview/1994.pdf.

[44] Purvis, J. C., Tyler, W. & Sidlow, S. Tropical storm chris 1988. Tech. Rep., South Carolina State Climatology Office (1988). URL https://www.dnr.sc.gov/climate/sco/hurricanes/pdfs/TropicalStormChris1988.pdf.

[45] Purvis, J. C., Tyler, W. & Sidlow, S. Hurricane charley (1986). Tech. Rep., South Carolina State Climatology Office (1987). URL https://www.dnr.sc.gov/climate/sco/hurricanes/pdfs/HurricaneCharley1986.pdf.

[46] Lawrence, M. B. Preliminary report: Hurricane gloria. Tech. Rep., National Hurricane Center (1985). URL http://atlas.amicale-des-ouragans.org/dossiers/gloria1985/1985_Gloria.pdf.

[47] Purvis, J. C. & Jarvinen, B. R. Hurricane david (1979). Tech. Rep., South Carolina State Climatology Office (1985). URL https://www.dnr.sc.gov/climate/sco/hurricanes/pdfs/HurricaneDavid1979.pdf.

[48] Knutson, T. R. *et al.* Global projections of intense tropical cyclone activity for the late twenty-first century from dynamical downscaling of cmip5/rcp4.5 scenarios. *J. Clim.* **28**, 7203–7224 (2015).

[49] Hou, H. *et al.* Resilience enhancement of distribution network under typhoon disaster based on two-stage stochastic programming. *Appl. Energy* **338**, 120892 (2023).

[50] Emanuel, K. & Rotunno, R. Self-stratification of tropical cyclone outflow. part i: Implications for storm structure. *J. Atmos. Sci.* **68**, 2236–2249 (2011).

[51] Xu, L., Lin, N., Xi, D., Feng, K. & Poor, H. V. Hazard resistance-based spatiotemporal risk analysis for distribution network outages during hurricanes. *IEEE Trans. Power Syst.* **40**, 2143–2152 (2025).

[52] Sun, S., Li, G., Chen, C., Bian, Y. & Bie, Z. A novel formulation of radiality constraints for resilient reconfiguration of distribution systems. *IEEE Trans. Smart Grid* **14**, 1337–1340 (2023).

[53] Woo, C. K. *et al.* Market-based estimation of average electricity outage costs in the united states. *Energy Res. Lett.* **5** (2024).

[54] Zuzak, C. National risk index technical documentation. Tech. Rep., Federal Emergency Management Agency (FEMA) (2025). URL https://www.fema.gov/sites/default/files/documents/fema_national-risk-index_technical-documentation.pdf.